Published OnlineFirst September 19, 2011; DOI:10.1158/1940-6207.CAPR-11-0290

reactions were done using the LightCycler 480 System (Roche Applied Science) following the manufacturer protocol. Fifty percent SYBR GREEN universal PCR Master Mix without UNG (Applied Biosystems), 50 nmol/L each of the forward and reverse primers and 2 μL of reversely transcribed cDNA were applied. Amplification conditions were 5 minutes at 95°C and then 45 cycles each consisting of 10 sec at 95°C, 1 minute at 55°C and 10 sec at 72°C. Then, reactions were heated for 15 sec at 95°C, 1 minute at 65°C to draw the melting curve, and cooled to 50°C for 10 seconds. Reaction conditions for target gene amplification were as described above and the equivalent of 5 ng of reverse transcribed RNA was used in each reaction. mRNA levels were normalized to *GAPDH* expression.

Immunohistochemistry and tissue microarray

Immunohistochemical analysis was done using anti-JMJD2B antibody (A301-478A; Bethyl Laboratories) as described previously (22). For clinical bladder and lung cancer tissue microarray, EnVision kit/horseradish peroxidase (HRP; Dako) was applied. Briefly, slides of paraffin-embedded tumor specimens were processed under high pressure (125°C, 30 seconds) in antigen-retrieval solution, high pH 9 (S2367; Dako), treated with peroxidase blocking regent, and then treated with protein blocking regent (X0909; Dako). Tissue sections were incubated with a rabbit anti-JMJD2B polyclonal antibody followed by secondary antibodies conjugated to peroxidase labeled dextran polymers (Dako). Antigen was visualized with substrate chromogen (Dako liquid DAB chromogen; Dako). Finally, tissue specimens were stained with Mayer's haematoxylin (Hematoxylin QS, Vector Laboratories) to discriminate the nucleus from the cytoplasm. Because the intensity of staining within each tumor tissue core was mostly homogeneous, the intensity of JMJD2B staining was semiquantitatively evaluated using the following criteria: negative (no appreciable staining in tumor cells) and positive (brown staining appreciable in more than 30% of the nucleus of tumor cells).

Immunocytochemistry

HeLa cells were transfected with pCAGGS-n3FC-JMJD2B. Forty-eight hours after transfection, cultured cells were fixed by 4% paraformaldehyde in 0.1 mol/L phosphate buffer (pH 7.4) at room temperature for 30 minutes and permeabilized with 0.5% Triton X-100 in PBS (Sigma). Fixed cells were blocked with 5% bovine serum albumin in PBS for 1 hour and incubated with primary antibodies overnight at 4°C. Then they were incubated with Alexa Fluor–conjugated second antibodies (Molecular Probes; Invitrogen) and observed using a Leica confocal microscopy (23).

siRNA transfection

siRNA oligonucleotide duplexes targeting the human *JMJD2B* transcripts were purchased from Sigma Genosys. siEGFP and siNegative control (siNC), which is a mixture of 3 different oligonucleotide duplexes, were used as control siRNAs. The siRNA sequences are described in Supplementary Table S2. siRNA duplexes (100 nmol/L final concentration) were transfected into bladder and lung cancer cell lines with Lipofectamine 2000 (Invitrogen), and cell viability was examined at indicated time points using the Cell Counting Kit-8 (Dojindo) and by colony formation assay as described previously (24).

Immunoblotting

Whole-cell lysates were prepared from the cells with radioimmunoprecipitation assay–like buffer, and total protein was transferred to nitrocellulose membrane. The membrane was probed with anti-JMJD2B antibody (H-200; Santa Cruz Biotechnology), anti-JMJD2B antibody (A301-478A; Bethyl Laboratories), anti-H3K9me3 (ab8898; Abcam), and anti-FLAG antibody (F7425; Sigma). ACTB (I-19; Santa Cruz Biotechnology) or histone H3 (ab1791, Abcam) was used to ensure equal loading and transfer of proteins. Protein bands were detected by incubating with HRP-conjugated antibodies (GE Healthcare) and visualizing with Enhanced Chemiluminescence (GE Healthcare).

Clonogenicity assays

NIH3T3 cells, cultured in DMEM 10% FBS, were transfected with a p3xFLAG-JMJD2B wild-type vector or a p3xFLAG-JMJD2B ΔJmjC mutant vector. The transfected NIH3T3 cells were cultured for 2 days and seeded in 10-cm dish at the density of 10,000 cells per 10-cm dish in triplicate. Subsequently, the cells were cultured in DMEM 10% FBS containing 0.9 (mg/mL) geneticin/G-418 for 2 weeks until colonies were visible. Colonies were stained with Giemsa (Merck) and counted by Colony Counter software.

Coupled cell-cycle and cell proliferation assay

A 5′-bromo-2′-deoxyuridine (BrdU) flow kit (BD Pharmingen) was used to determine the cell-cycle kinetics and to measure the incorporation of BrdU into DNA of proliferating cells (25, 26). The assay was done according to the manufacturer protocol. Briefly, cells (2×10^5 per well) were seeded overnight in 6-well tissue culture plates and treated with an optimized concentration of siRNAs in medium containing 10% FBS for 72 hours, followed by addition of 10 μmol/L BrdU and incubations continued for an additional 30 minutes. Both floating and adherent cells were pooled from triplicate wells per treatment point, fixed in a solution containing paraformaldehyde and the detergent saponin, and incubated for 1 hour with DNase at 37°C (30 μg per sample). Fluorescein isothiocyanate (FITC)-conjugated anti-BrdU antibody (1:50 dilution in wash buffer; BD Pharmingen) was added and incubation continued for 20 minutes at room temperature. Cells were washed in wash buffer and total DNA was stained with 7-amino-actinomycin D (7-AAD; 20 μL per sample), followed by flow cytometric analysis using FACScan (Beckman Coulter) and total DNA content (7-AAD) was determined using CXP Analysis Software Ver. 2.2 (Beckman Coulter).

Published OnlineFirst September 19, 2011; DOI:10.1158/1940-6207.CAPR-11-0290

Microarray hybridization and statistical analysis for the clarification of downstream genes

Microarray analysis to identify downstream genes were done as described previously (21). Purified total RNA was labeled and hybridized onto Affymetrix GeneChip U133 Plus 2.0 oligonucleotide arrays (Affymetrix) according to the manufacturer instructions. Probe signal intensities were normalized by RMA and Quantile (using R and Bioconductor). Because we could also confirm the microarray data of several randomly selected candidate genes using quantitative real-time PCR (Supplementary Fig. S4D), we assume our microarray data are reliable.

Chromatin immunoprecipitation assay

Chromatin immunoprecipitation (ChIP) assays were done using ChIP Assay kit (Millipore) according to the manufacturer protocol. Briefly, the fragment of JMJD2B and chromatin complexes was immunoprecipitated with anti-FLAG antibody 48 hours after transfection with pCAGGS-n3FC (mock) and pCAGGS-n3FC-JMJD2B vectors into 293T cells. After the bound DNA fragments to JMJD2B were eluted, a standardized amount was subjected to quantitative real-time PCR reactions. Primer sequences are shown in Supplementary Table S1.

Results

Overexpression of JMJD2B in clinical bladder and lung cancer tissues

We first examined expression levels of a number of jumonji histone demethylase genes in a small subset of clinical bladder cancer samples and found significant differences in expression levels between normal and cancer cells for the *JMJD2B* gene (data not shown). Then, we analyzed 76 bladder cancer samples and 20 normal control samples (British) and found significantly higher expression levels of *JMJD2B* in bladder cancer tissues compared with normal bladder ($P < 0.0001$, Mann–Whitney *U* test; Fig. 1A and B). Subclassification of tumors according to tumor grade, metastasis status, recurrence status, and smoking history identified no significant differences, whereas gender was significant ($P < 0.0001$, Mann–Whitney *U* test; Supplementary Table S3). Importantly, JMJD2B was notably overexpressed at an early stage of bladder cancer (Supplementary Fig. S1). Next, we evaluated JMJD2B protein expression levels in bladder tissues. After confirming the specificity of the antibody we used (Supplementary Fig. S2), we carried out immunohistochemistry using the specific JMJD2B antibody. This experiment showed strong nuclear staining of JMJD2B, specifically in bladder cancer tissues, whereas no significant staining was observed in normal bladder tissues (Fig. 1C). Among 29 bladder cancer tissue sections, 20 showed positive staining of JMJD2B (70.0%; Supplementary Table S4). In addition, our microarray expression analysis of a number of clinical samples indicated that *JMJD2B* was overexpressed in lung cancer (Fig. 2A and B). According to immunohistochemical analysis using clinical lung tissues, nuclear staining of JMJD2B was observed in cancer tissues, although no significant nuclear staining was evaluated in normal lung and placental tissues (Fig. 2B). Of 63 lung cancer cases, JMJD2B stained positively in 24 cases (38.1%; Supplementary Table S5).

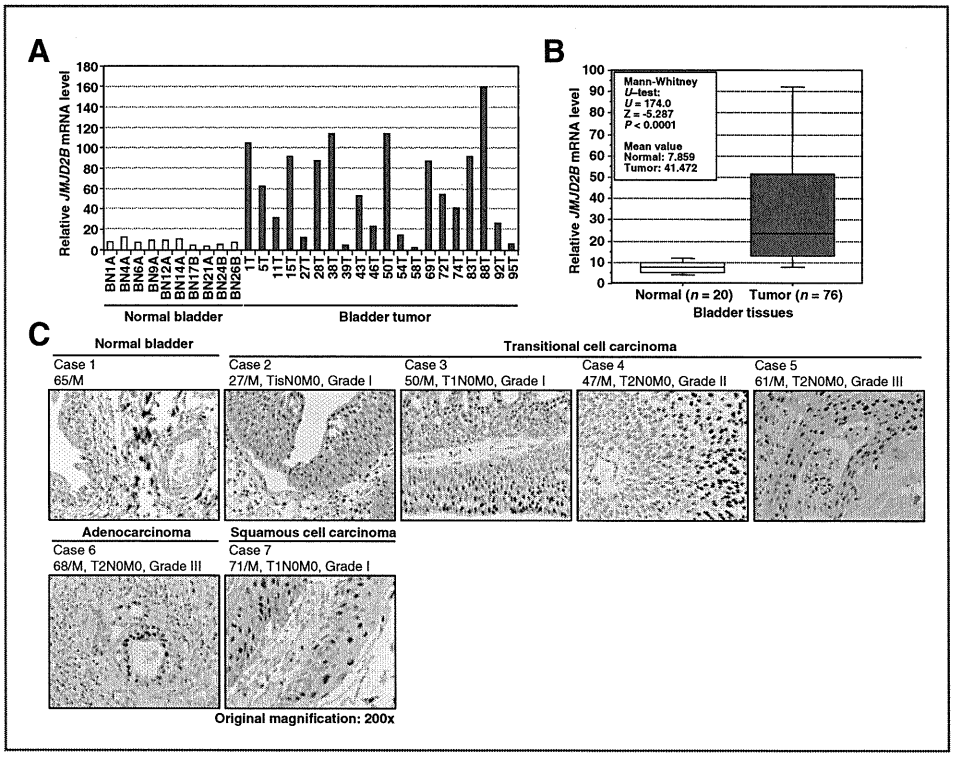

Figure 1. Overexpression of JMJD2B in clinical bladder cancers. A, mRNA levels of *JMJD2B* in representative cases of clinical normal bladder tissues and bladder cancer tissues (British). B, quantitative real-time PCR measurements were carried out using 76 bladder cancer samples and 20 normal bladder samples, and the result is shown by box-whisker plot. For statistical analysis, the Mann–Whitney *U* test was adopted (mean: 41.47 (tumor) versus 7.86 (normal), $P < 0.0001$). C, immunohistochemical analysis of JMJD2B in bladder tissues. Clinical information for each section is represented above histologic pictures. All tissue samples were purchased from BioChain. Original magnification: ×200.

Published OnlineFirst September 19, 2011; DOI:10.1158/1940-6207.CAPR-11-0290

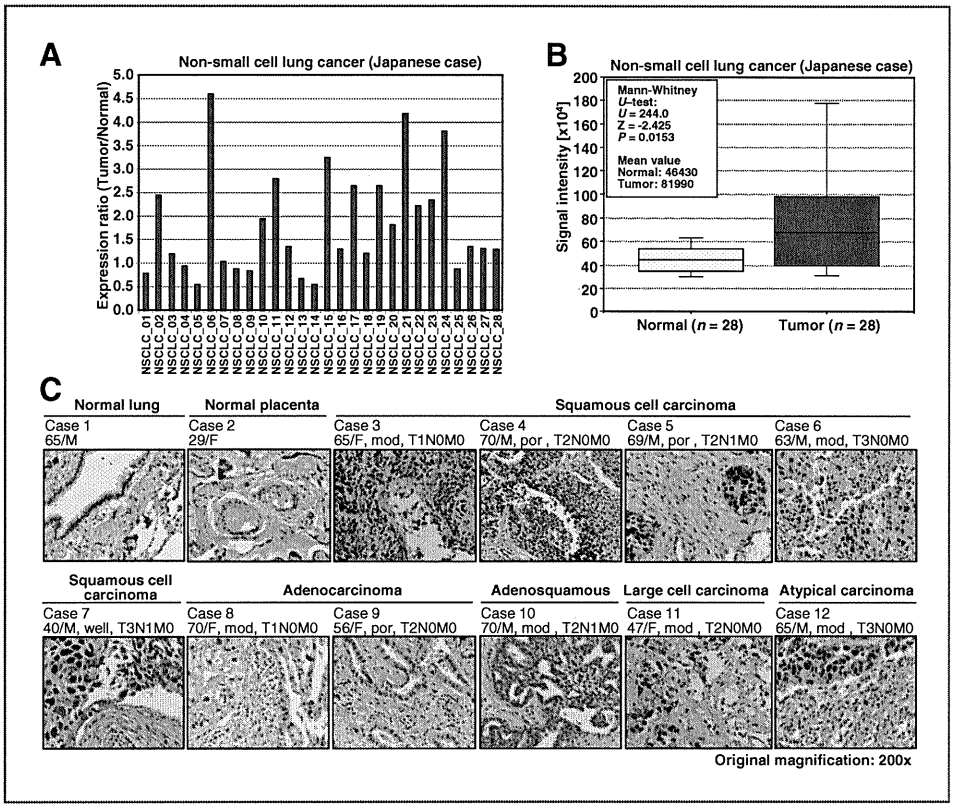

Figure 2. Elevated expression of JMJD2B in lung cancer tissues. A, expression ratio between normal lung and non–small cell lung cancer (NSCLC) tissues. Signal intensity for each sample was analyzed by cDNA microarray, and the expression ratio is the signal intensity in tumor divided by that in normal (1 is normal). B, comparison of *JMJD2B* expression between normal and tumor (NSCLC) lung tissues in Japanese patients. Signal intensity for each sample was analyzed by cDNA microarray, and the result is shown by box-whisker plot (median 50% boxed). Mann–Whitney *U*-test was used for the statistical analysis. C immunohistochemical analysis of JMJD2B in normal and lung cancer tissues. Clinical information for each section is represented above histologic pictures. All tissue samples were purchased from BioChain. Original magnification: ×200.

Together, expression levels of JMJD2B in bladder and lung cancer tissues are significantly higher than those in corresponding nonneoplastic tissues at the mRNA and protein levels.

JMJD2B plays an essential role in the growth regulation of cancer cells

To determine the significance of JMJD2B in human carcinogenesis, we examined whether JMJD2B is involved in the growth regulation of cancer cells. After confirming the elevated expression of JMJD2B in bladder and lung cancer cell lines, compared with the human airway epithelial cell line SAEC and the colonic fibroblast cell line CCD-18Co at the protein level (Fig. 3A), we inhibited JMJD2B expression in SW780 and A549 cells using 2 different siRNA oligonucleotide duplexes (Supplementary Table S2). As shown in Fig. 3B, the specific siRNAs clearly knocked down JMJD2B expression, and subsequently, we carried out a cell growth assay 72 hours after treatment with the same siRNAs. JMJD2B knockdown significantly suppressed growth of bladder and lung cancer cells (Fig. 3C), and this result was also confirmed by a colony formation assay (Fig. 3D). Similarly, growth suppression effect was confirmed in the other bladder cancer cell line SCaBER (Supplementary Fig. S3A and B). We then conducted BrdU and 7-AAD staining to analyze the detailed cell-cycle status of cancer cells after the knockdown of JMJD2B and confirmed that the proportion of cancer cells at the S phase was significantly decreased (Fig. 4A). Concomitantly, the percentage of cancer cells at G_1 phase significantly increased, indicating that JMJD2B could be a critical factor in the regulation of the G_1–S transition in cancer cells. These results suggested that JMJD2B plays an essential role in the growth regulation of cancer cells by modulating the G_1–S transition.

To examine the oncogenic activity of JMJD2B in more detail, we conducted a clonogenicity assay. A JMJD2B expression vector was constructed, capable of driving production of active enzyme within transfected cell lines (Fig. 4B). A wild-type JMJD2B (JMJD2B Wt) vector and an enzyme-dead JMJD2B (JMJD2B ΔJmjC) version of our vector were transfected into separate cultures of NIH3T3 cells. A clonogenicity assay was done on each culture (Fig. 4C; Materials and Methods). Wild-type JMJD2B protein showed stronger oncogenic activity than enzyme-dead JMJD2B protein; therefore, it is the demethylase activity of JMJD2B that promotes oncogenesis in cells. Because JMJD2B is overexpressed at an early stage in cancer progression, JMJD2B seems to play a crucial role in human carcinogenesis.

JMJD2B promotes cell-cycle progression through the regulation of cyclin-dependent kinase 6

We next analyzed downstream genes and pathways associated with JMJD2B to clarify the mechanism by which JMJD2B regulates cell-cycle progression. After treatment with *JMJD2B* siRNA in SW780 and A549, we carried out Affymetrix GeneChip analysis. To exclude the secondary effects of growth suppression, we picked statistically

Published OnlineFirst September 19, 2011; DOI:10.1158/1940-6207.CAPR-11-0290

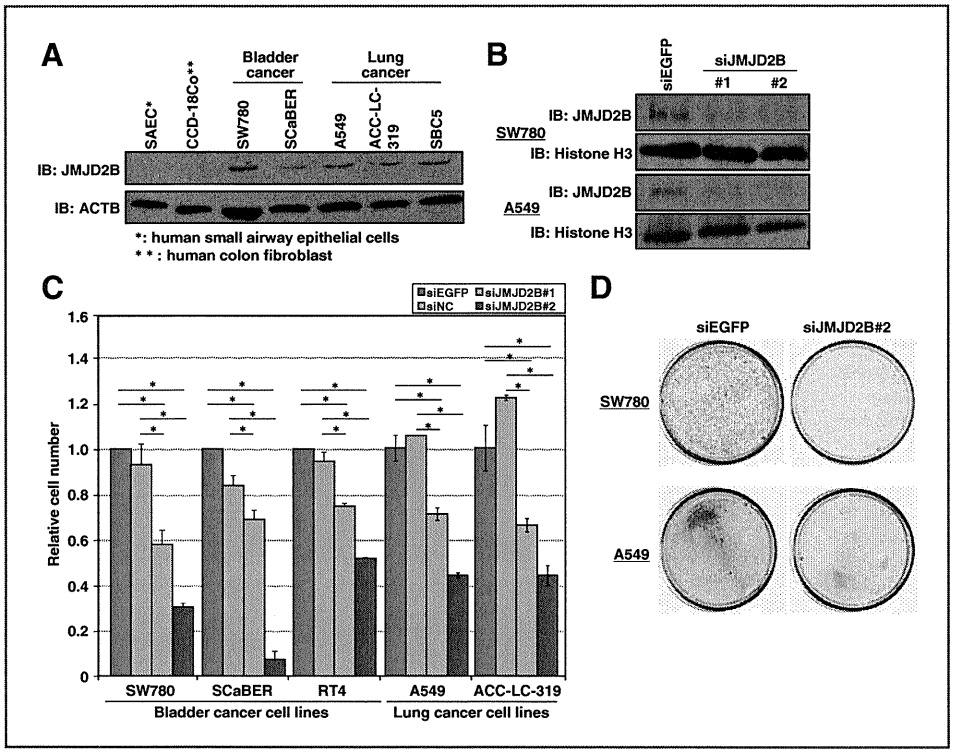

Figure 3. Knockdown of JMJD2B expression leads to significant growth suppression of cancer cells. A, validation of JMJD2B protein expression levels in various cell lines. Lysates from the human airway epithelial cell line (SAEC), the colonic fibroblast cell line (CCD-18Co), 2 bladder cancer cell lines (SW780 and SCaBER) and 3 lung cancer cell lines (A549, ACC-LC-319, and SBC5) were immunoblotted with antibodies against JMJD2B and ACTB (an internal control). B, validation of JMJD2B knockdown at the protein level. Lysates from SW780 and A549 cells 72 hours after siRNA treatment were immunoblotted with anti-JMJD2B and anti-histone H3 (an internal control) antibodies. C, effects of JMJD2B knockdown on the proliferation of bladder and lung cancer cell lines (SW780, SCaBER, RT4, A549, and ACC-LC-319) measured by Cell Counting kit 8. Relative cell numbers are normalized to the number of siEGFP-treated cells (siEGFP = 1): results are the mean ± SD of 3 independent experiments. *P* values were calculated using Student *t* test (*, $P < 0.05$). D, colony formation assay of SW780 and A549 cells. Giemsa staining was done 5 days (SW780) and 3 days (A549) after treatment with siRNAs. IB, immunoblotting.

significant signals which were commonly decreased at 12 and 24 hours after siRNA treatment. The knockdown of JMJD2B was clearly confirmed at the protein level (Fig. 5A, right top). Among candidate genes, we observed a significant downregulation of cyclin-dependent kinase 6 (CDK6), one of the key regulators for the G_1–S transition (Fig. 5A, left and right bottom and Supplementary Fig. S4A; ref. 27). Quantitative real-time PCR also confirmed a significant downregulation of *CDK6* at both 12 and 48 hours following *JMJD2B* siRNA treatment (Fig. 5B and Supplementary Fig. S4B). Likewise, downregulation of CDK6 after JMJD2B knockdown was confirmed at the protein level (Supplementary Fig. S4C). In addition, we confirmed a significant elevation of *CDK6* in HeLa cells transfected with pCAGGS-n3FC-JMJD2B compared with mock-treated cells (Fig. 5C). To evaluate the possibility that JMJD2B directly regulates CDK6 expression at the transcriptional level, we conducted a ChIP assay. JMJD2B protein was highly enriched at the promoter region of CDK6 after transfection with a pCAGGS-n3FC-JMJD2B vector, accompanied by decreased levels of H3-K9 trimethylation in the region (Fig. 5D). Consistently, signal pathway analysis using the Gene Ontology database indicated that JMJD2B can regulate cell-cycle checkpoint pathways, as well as other important pathways involved in carcinogenesis (Supplementary Table S6). The data revealed that JMJD2B directly activates the expression of CDK6 through demethylation of histone H3 at lysine 9.

Because it is well-known that p16INK4a is an important regulator of CDK6 (28–32), we examined the relationship between p16INK4A and JMJD2B in regulating CDK6. To compare expression levels of *p16INK4a*, *JMJD2B*, and *CDK6*, we conducted quantitative real-time PCR analysis on 14 different cell lines (Fig. 6A). Although p16INK4A is considered an important inactivator of CDK6, we did not find a significant inverse correlation between *p16INK4a* and *CDK6* expressions; instead, a slight positive correlation was observed (Fig. 6B, left). This implies that p16INK4a is unlikely to regulate transcription levels of *CDK6* to inactivate the cell-cycle dependent-kinase. On the contrary, expression levels of *JMJD2B* and *CDK6* were significantly positively correlated in 14 cell lines (Fig. 6B, right), which is consistent with our results (Fig. 5). Intriguingly, expression levels of *JMJD2B* and *CDK6* were strongly correlated in cell lines expressing low levels of *p16INK4a* (Fig. 6C; $r = 0.976$, $P < 0.0001$). According to our data, JMJD2B-dependent transcriptional

Published OnlineFirst September 19, 2011; DOI:10.1158/1940-6207.CAPR-11-0290

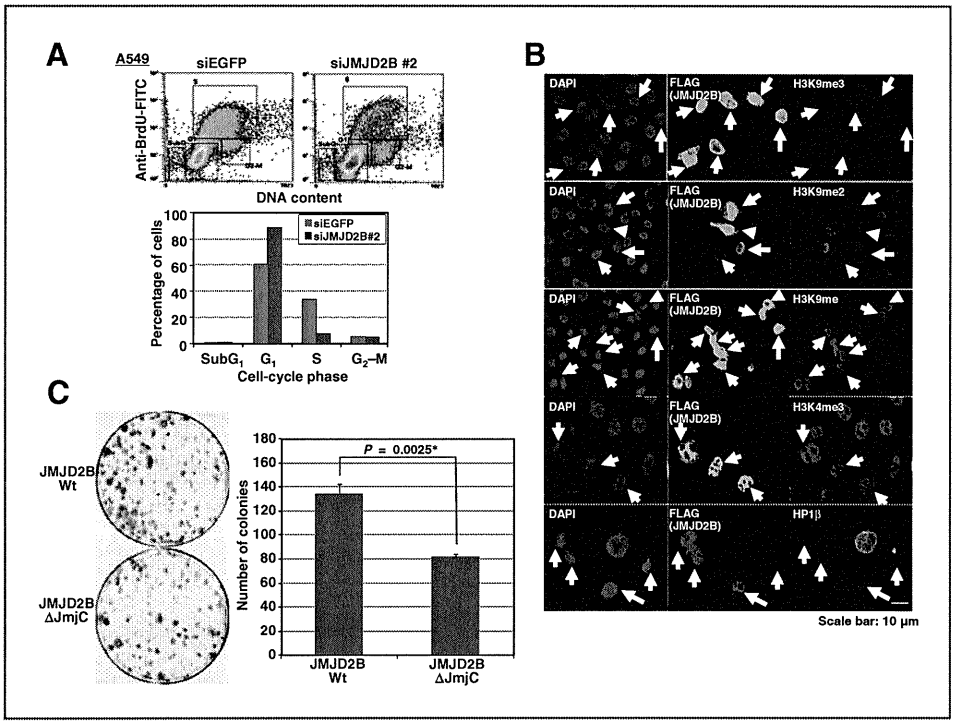

Figure 4. Fluorescence-activated cell sorting (FACS) and clonogenicity analyses. A, effects of JMJD2B knockdown on cell-cycle kinetics in cancer cells. A549 cells were collected 72 hours after treatment with siRNAs, and cell-cycle distribution was analyzed by flow cytometry after coupled staining with FITC-conjugated anti-BrdU and 7-AAD, described in Materials and Methods. Representative histograms of the FACS results (top) and numerical analysis (bottom) are shown for each experiment. B, validation of subcellular localization and an enzymatic activity of JMJD2B. 3xFLAG-JMJD2B transfected HeLa cells were stained for specific antibodies as indicated above. Immunostaining showed nuclear localization of JMJD2B and its reversing activity against tri- and di-methylated H3K9, accompanied with the increased signal of H3K9me and the decreased signal of Hp1beta. Scale bar denotes 10μm. DAPI, 4′, 6-diamidino-2-phenylindole. C, clonogenicity assays of NIH3T3 cells. Cells transfected with a 3xFLAG-JMJD2B vector and a 3xFLAG-JMJD2B ΔJmjC were cultured in DMEM 10% FBS containing 0.9 (mg/mL) geneticin/G-418 for 2 weeks and colonies were stained with Giemsa.

regulation of *CDK6* seems to be affected by expression levels of *p16INK4a*.

Discussion

Among posttranslational modifications on histones, methylation has been shown to be involved in transcriptional regulation, such as X-inactivation or genomic imprinting (1, 2). Although it had been unclear whether histone methylation marks could be reversed, LSD1, a flavin-dependent amine oxidase histone demethylase, was identified as the first histone demethylase (4). Unlike LSD1, the JmjC family, harboring the conserved JmjC domain, require Fe (II) and α-ketoglutarate to exert demethylase activity, and this demethylation process results in the generation of formaldehyde and succinate (7). Among these enzymes, the JMJD2 family demethylate H3K9 and H3K36 (6), and JMJD2B selectively removes H3K9me2 and H3K9me3 (15, 17). Functional studies showed that JMJD2B contains hypoxia response elements in its promoter region and, therefore, JMJD2B is induced by Hypoxia-inducible factor (HIF; refs. 16, 17), but its significance in human diseases such as cancer remains to be elucidated. In this study, we showed significant upregulation of JMJD2B in various types of cancers, including bladder and lung, by quantitative real-time PCR, cDNA microarray, or immunohistochemistry. In addition, a series of our experiments clarified that JMJD2B serves a critical role in the growth regulation of cancer cells, especially at the G_1–S transition (Fig. 3 and Supplementary Fig. S3). This JMJD2B-dependent cell-cycle regulation could be mediated by the downstream gene *CDK6* through the demethylation of histone H3-K9 at the promoter region (Fig. 5), indicating that the enzyme activity of JMJD2B may be an important regulator for the G_1–S transition in cancer cells. Expression analysis examining the correlation between JMJD2B and the histone methyltransferase G9a, catalyzing histone H3-K9 methylation, showed that *G9a* expression was not changed after treatment with JMJD2B siRNA (Supplementary Fig. S5). We interpret this to mean that although both proteins regulate the methylation status of histone H3K9, the target genes may be different. In fact, we have recently published a paper analyzing the significance of G9a deregulation in human carcinogenesis (33). We reported that G9a is overexpressed in various types of cancer, similarly to JMJD2B. Our functional analyses showed that G9a and JMJD2B may regulate different genes (our previous data in ref. 33 and Supplementary Table S6). Therefore, the histone demethylase JMJD2B and the histone methyltransferase G9a

Published OnlineFirst September 19, 2011; DOI:10.1158/1940-6207.CAPR-11-0290

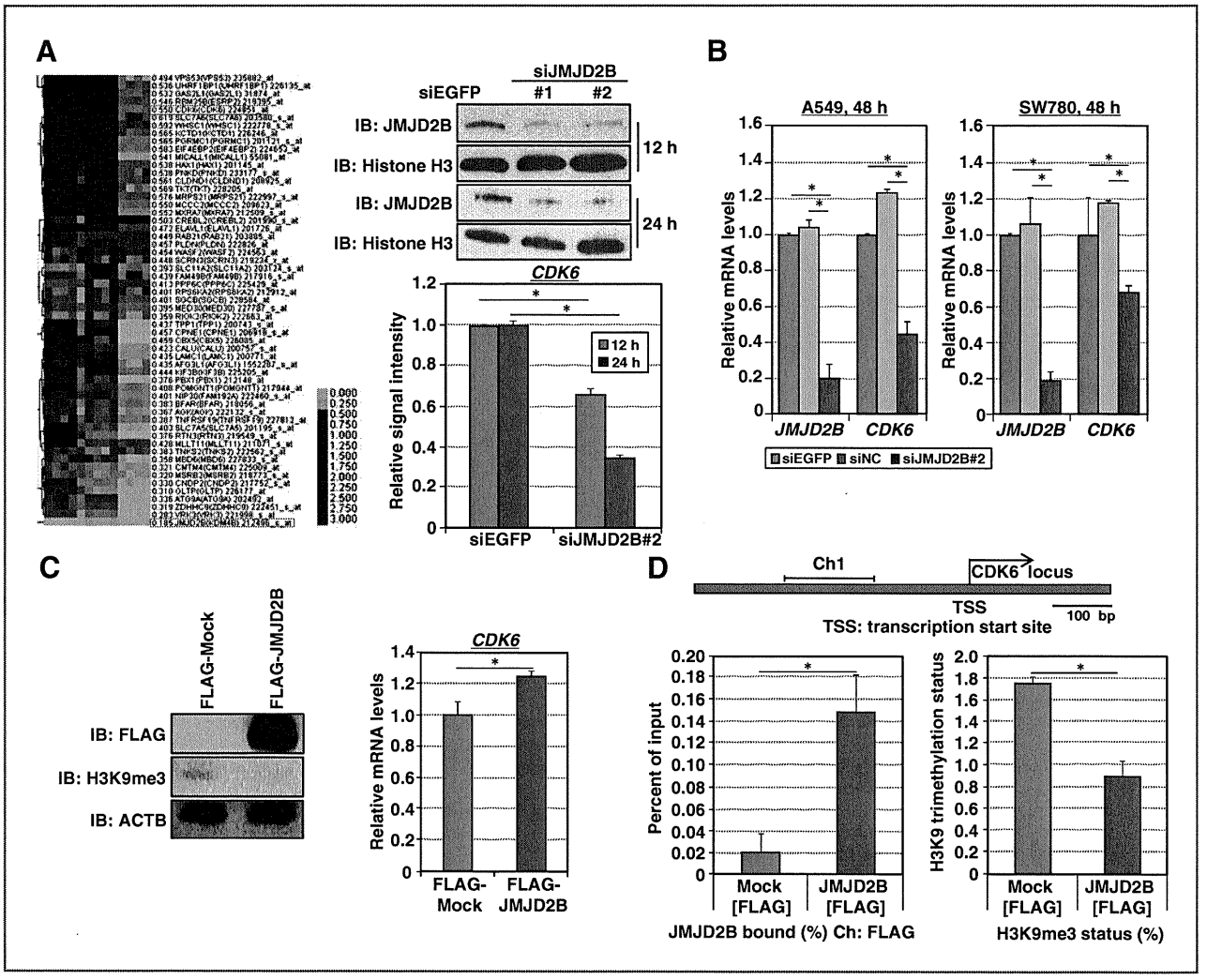

Figure 5. JMJD2B transcriptionally activates CDK6 expression through demethylation of H3K9me3 at the promoter region. A, left, 2-dimensional, unsupervised hierarchical cluster analysis of SW780 and A549 mRNA expression profiles after knockdown of *JMJD2B* expression. Differentially expressed genes were selected for this analysis. Right top, validation of JMJD2B knockdown at the protein level. Lysates from SW780 cells 12 and 24 hours after siRNA treatment were immunoblotted with anti-JMJD2B and anti-histone H3 (an internal control) antibodies. Right bottom, signal intensity of *CDK6* in SW780 cells after treatment with siEGFP (control) and siJMJD2B#2 was quantified by GeneChip U133 plus 2.0 (Affymetrix). B, relative *CDK6* mRNA levels in A549 and SW780 cells 48 hours after treatment with siEGFP, siNC, and siJMJD2B#2 were analyzed by quantitative real-time PCR. Results are the mean ± SD in 3 independent experiments, and the *P* value was calculated using Student *t* test (*, $P < 0.05$). C, HeLa cells transfected with pCAGGS-n3FC-mock or pCAGGS-n3FC-JMJD2B were collected 48 hours after the transfection. Left, the samples were fractionated by SDS-PAGE and immunoblotted with anti-FLAG, anti-H3K9me3 and anti-ACTB (an internal control) antibodies. Right, relative *CDK6* mRNA levels were analyzed by quantitative real-time PCR. Results are the mean ± SD in 3 independent experiments, and the *P* value was calculated using Student *t* test (*, $P < 0.05$). D, ChIP assay for JMJD2B at the promoter region of *CDK6* gene. Top, a schematic diagram of the *CDK6* promoter region. The PCR amplified fragment is positioned by nucleotide number relatives to TSS (arrow). Left bottom, quantitative real-time PCR analysis using a primer pair as described in Materials and Methods. Cross-linked and sheared chromatin was immunoprecipitated with anti-FLAG antibody (M2, Sigma). The result is shown as a percentage of the input chromatin. Right bottom, quantification of H3K9me3 ChIP at the *CDK6* promoter region using quantitative real-time PCR. Cross-linked and sheared chromatin was immunoprecipitated with an anti-H3K9me3 antibody (ab8898; Abcam). IB, immunoblotting.

both regulate the status of histone H3K9 methylation and play important roles in human carcinogenesis but may regulate different pathways.

CDK6 is a member of the cyclin-dependent protein kinase family and a catalytic subunit of the protein kinase complex that is important for cell-cycle regulation. This kinase promotes cell-cycle progression from G_1 phase to S phase through promoting RB phosphorylation and subsequent detachment of E2F1 from RB (27). CDK6 has been reported to possess various physiologic functions like T-cell development (34, 35). Importantly, our microarray data showed the aberrant expression of *CDK6* in several types of human tumors, including bladder and lung cancers (Supplementary Table S7), and previous reports also described

Published OnlineFirst September 19, 2011; DOI:10.1158/1940-6207.CAPR-11-0290

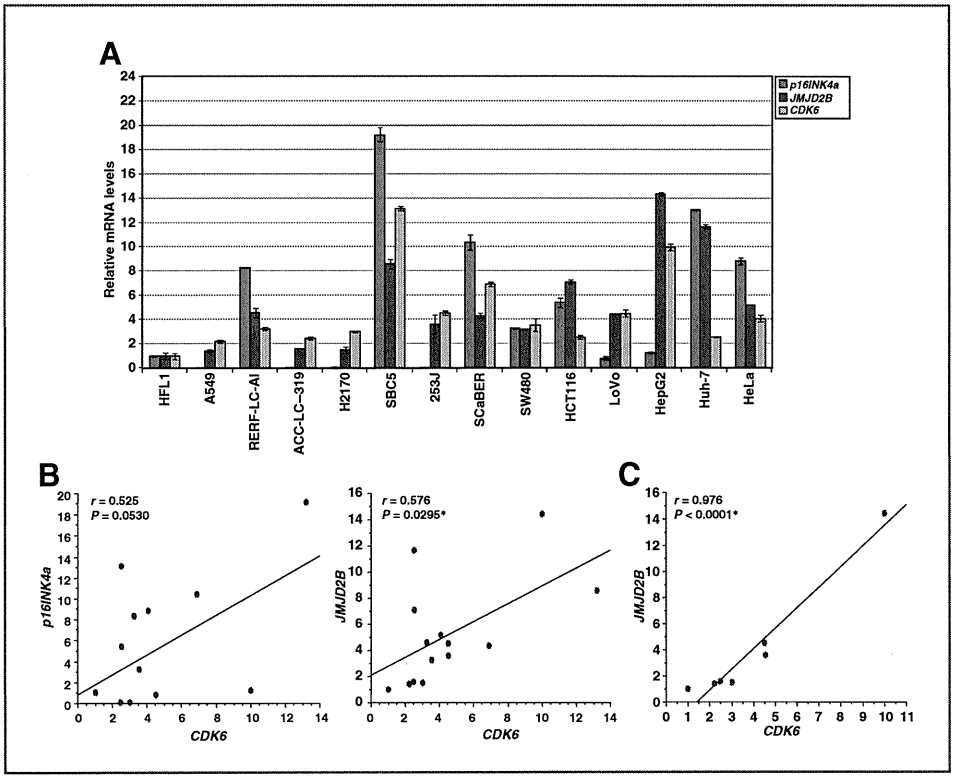

Figure 6. *JMJD2B* and *CDK6* expressions are significantly correlated in various types of cell lines. A, quantitative real-time PCR analysis of one normal cell line (HFL1), 5 lung cancer cell lines (A549, RERF-LC-AI, ACC-LC-319, H2170, and SBC5), 2 bladder cell lines (253J and SCaBER), 3 colorectal cancer cell lines (SW480, HCT116, and LoVo), 2 liver cancer cell lines (HepG2 and Huh-7), and 1 cervical cancer cell line. Expression levels of *p16INK4a*, *JMJD2B* and *CDK6* were examined. mRNA expression levels were normalized to *GAPDH*, and values are relative to HFL1. B, correlation among *p16INK4a*, *JMJD2B*, and *CDK6* expressions in 14 cell lines analyzed by quantitative real-time PCR. Pearson *r* correlation was used to measure the relationship between the expression of the 2 genes. C, correlation between *JMJD2B* and *CDK6* expressions in 7 cell lines expressing low levels of *p16INK4a* (HFL1, A549, ACC-LC-319, H2170, 253J, LoVo, and HepG2) analyzed by quantitative real-time PCR. Pearson *r* correlation was used to measure the expression of relationship between the expression of the 2 genes.

the involvement of this gene in human carcinogenesis (27, 35, 36). This study shows that CDK6 is transcriptionally activated by JMJD2B through demethylation of H3K9 and that elevated CDK6 is likely to promote cell malignancy. This is a novel example of how deregulated histone demethylation contributes to human carcinogenesis. To date, the tumor suppressor gene *p16INK4a* has been considered as an important negative regulator of CDK6 through direct interaction (30, 37). We found that an inverse correlation was not observed between *p16INK4a* and *CDK6* expressions, and that *JMJD2B* expression was strongly correlated to *CDK6* expression, especially in cell lines expressing low levels of *p16INK4a*. These results indicate that expression levels of *p16INK4a* are likely to be a regulator of JMJD2B-dependent *CDK6* transcriptional activation. Further functional analysis is required to clarify the crosstalk between the JMJD2B-CDK6 and the p16INK4a-RB1 pathways.

Detailed expression analysis showed that expression levels of JMJD2B in bladder and lung cancers are significantly higher than those in corresponding normal tissues, and knockdown of JMJD2B resulted in the significant suppression of cancer cell proliferation. To explain the mechanism for increased expression of JMJD2B in human cancers, we looked at the genome annotation across the *JMJD2B* region, spanning Ch19 4,806,367 to 5,154,791 using the 1 Mb CGH array data of bladder cancer tissues. There are no single gains or amplifications; therefore, we cannot confirm there is a gain relating to gene dosage in bladder cancer. Beyer and colleagues previously reported that the HIF-1α binds to specific recognition sites in the gene encoding *JMJD2B* and induces its expression (17). All human tumors display genomic instability, aberrant transcriptional programs, and, very often, contain areas that are insufficiently perfused, resulting in a local shortage of nutrients and oxygen (hypoxia). This leads to an activation of the transcription factor HIF, the master regulator of oxygen homeostasis (38). These results imply that low-oxidation concentration in cells seems to be an important mediator in activating JMJD2B expression in human carcinogenesis. In addition, the Oncomine database (39) implies that JMJD2B is overexpressed in various types of cancer (Supplementary Fig. S6), so deregulation of JMJD2B plainly contributes to carcinogenesis in a variety of human tumor types. Importantly, expression levels of JMJD2B in various

Published OnlineFirst September 19, 2011; DOI:10.1158/1940-6207.CAPR-11-0290

types of normal tissues are significantly low (Supplementary Fig. S7). These results indicate JMJD2B as an ideal target for cancer therapy. Our functional analyses were mainly based on *in vitro* models, so additional data from animal experimental models may reinforce the importance of JMJD2B as a therapeutic target in human cancer. Recently, inhibitors targeting DNA methyltransferases and histone deacetylases were approved by the FDA to use for patients with hematologic malignancies (40, 41). Furthermore, a novel inhibitor targeting the histone demethylase LSD1 has been developed and a suppressive effect on tumor growth, via reexpression of epigenetically silenced genes in colon cancer cells, was shown (42). On the basis of these results, it seems feasible to develop specific inhibitors targeting JMJD2B as anticancer agents. Because the development of inhibitors targeting histone methyltransferases and demethylases has begun, these reagents should be further validated against the functions of this enzyme, to assure the usefulness of this approach in the near future.

Disclosure of Potential Conflicts of Interest

No potential conflicts of interest were disclosed.

Acknowledgments

The authors thank Professor Gillian Murphy and the members of her laboratory for substantial technical support and also thank Ms. Yuka Yamane and Ms. Haruka Sawada for technical assistance.

Grant Support

This work was supported by a grant-in aid for young scientists (A; 22681030) from the Japan Society for the Promotion of Science. Our biorepository is supported by funding NIHR and the Cambridge Biomedical Research Centre.

The costs of publication of this article were defrayed in part by the payment of page charges. This article must therefore be hereby marked *advertisement* in accordance with 18 U.S.C. Section 1734 solely to indicate this fact.

Received June 3, 2011; revised August 16, 2011; accepted September 2, 2011; published OnlineFirst September 19, 2011.

References

1. Jenuwein T, Allis CD. Translating the histone code. Science 2001;293:1074–80.
2. Kouzarides T. Chromatin modifications and their function. Cell 2007;128:693–705.
3. Peterson CL, Laniel MA. Histones and histone modifications. Curr Biol 2004;14:R546–51.
4. Shi Y, Lan F, Matson C, Mulligan P, Whetstine JR, Cole PA, et al. Histone demethylation mediated by the nuclear amine oxidase homolog LSD1. Cell 2004;119:941–53.
5. Bannister AJ, Kouzarides T. Reversing histone methylation. Nature 2005;436:1103–6.
6. Whetstine JR, Nottke A, Lan F, Huarte M, Smolikov S, Chen Z, et al. Reversal of histone lysine trimethylation by the JMJD2 family of histone demethylases. Cell 2006;125:467–81.
7. Tsukada Y, Fang J, Erdjument-Bromage H, Warren ME, Borchers CH, Tempst P, et al. Histone demethylation by a family of JmjC domain-containing proteins. Nature 2006;439:811–6.
8. Hamamoto R, Furukawa Y, Morita M, Iimura Y, Silva FP, Li M, et al. SMYD3 encodes a histone methyltransferase involved in the proliferation of cancer cells. Nat Cell Biol 2004;6:731–40.
9. Hamamoto R, Silva FP, Tsuge M, Nishidate T, Katagiri T, Nakamura Y, et al. Enhanced SMYD3 expression is essential for the growth of breast cancer cells. Cancer Sci 2006;97:113–8.
10. Silva FP, Hamamoto R, Kunizaki M, Tsuge M, Nakamura Y, Furukawa Y. Enhanced methyltransferase activity of SMYD3 by the cleavage of its N-terminal region in human cancer cells. Oncogene 2008;27:2686–92.
11. Sparmann A, van Lohuizen M. Polycomb silencers control cell fate, development and cancer. Nat Rev Cancer 2006;6:846–56.
12. Takeshita F, Minakuchi Y, Nagahara S, Honma K, Sasaki H, Hirai K, et al. Efficient delivery of small interfering RNA to bone-metastatic tumors by using atelocollagen *in vivo*. Proc Natl Acad Sci U S A 2005;102:12177–82.
13. Schneider R, Bannister AJ, Kouzarides T. Unsafe SETs: histone lysine methyltransferases and cancer. Trends Biochem Sci 2002;27:396–402.
14. Katoh M. Identification and characterization of JMJD2 family genes *in silico*. Int J Oncol 2004;24:1623–8.
15. Fodor BD, Kubicek S, Yonezawa M, O'Sullivan RJ, Sengupta R, Perez-Burgos L, et al. Jmjd2b antagonizes H3K9 trimethylation at pericentric heterochromatin in mammalian cells. Genes Dev 2006;20:1557–62.
16. Pollard PJ, Loenarz C, Mole DR, McDonough MA, Gleadle JM, Schofield CJ, et al. Regulation of Jumonji-domain-containing histone demethylases by hypoxia-inducible factor (HIF)-1alpha. Biochem J 2008;416:387–94.
17. Beyer S, Kristensen MM, Jensen KS, Johansen JV, Staller P. The histone demethylases JMJD1A and JMJD2B are transcriptional targets of hypoxia-inducible factor HIF. J Biol Chem 2008;283:36542–52.
18. Wallard MJ, Pennington CJ, Veerakumarasivam A, Burtt G, Mills IG, Warren A, et al. Comprehensive profiling and localisation of the matrix metalloproteinases in urothelial carcinoma. Br J Cancer 2006;94:569–77.
19. Olsburgh J, Harnden P, Weeks R, Smith B, Joyce A, Hall G, et al. Uroplakin gene expression in normal human tissues and locally advanced bladder cancer. J Pathol 2003;199:41–9.
20. Kitahara O, Furukawa Y, Tanaka T, Kihara C, Ono K, Yanagawa R, et al. Alterations of gene expression during colorectal carcinogenesis revealed by cDNA microarrays after laser-capture microdissection of tumor tissues and normal epithelia. Cancer Res 2001;61:3544–9.
21. Yoshimatsu M, Toyokawa G, Hayami S, Unoki M, Tsunoda T, Field HI, et al. Dysregulation of PRMT1 and PRMT6, Type I arginine methyltransferases, is involved in various types of human cancers. Int J Cancer 2011;128:562–73.
22. Toyokawa G, Masuda K, Daigo Y, Cho HS, Yoshimatsu M, Takawa M, et al. Minichromosome maintenance protein 7 is a potential therapeutic target in human cancer and a novel prognostic marker of non-small cell lung cancer. Mol Cancer 2011;10:65.
23. Cho HS, Suzuki T, Dohmae N, Hayami S, Unoki M, Yoshimatsu M, et al. Demethylation of RB regulator MYPT1 by histone demethylase LSD1 promotes cell cycle progression in cancer cells. Cancer Res 2011;71:1–6.
24. Sato N, Yamabuki T, Takano A, Koinuma J, Aragaki M, Masuda K, et al. Wnt inhibitor Dickkopf-1 as a target for passive cancer immunotherapy. Cancer Res 2010;70:5326–36.
25. Hayami S, Kelly JD, Cho HS, Yoshimatsu M, Unoki M, Tsunoda T, et al. Overexpression of LSD1 contributes to human carcinogenesis through chromatin regulation in various cancers. Int J Cancer 2011;128:574–86.
26. Hayami S, Yoshimatsu M, Veerakumarasivam A, Unoki M, Iwai Y, Tsunoda T, et al. Overexpression of the JmjC histone demethylase KDM5B in human carcinogenesis: involvement in the proliferation

Published OnlineFirst September 19, 2011; DOI:10.1158/1940-6207.CAPR-11-0290

of cancer cells through the E2F/RB pathway. Mol Cancer 2010; 9:59.
27. Senderowicz AM. Small-molecule cyclin-dependent kinase modulators. Oncogene 2003;22:6609–20.
28. Alcorta DA, Xiong Y, Phelps D, Hannon G, Beach D, Barrett JC. Involvement of the cyclin-dependent kinase inhibitor p16 (INK4a) in replicative senescence of normal human fibroblasts. Proc Natl Acad Sci U S A 1996;93:13742–7.
29. Fahraeus R, Paramio JM, Ball KL, Lain S, Lane DP. Inhibition of pRb phosphorylation and cell-cycle progression by a 20-residue peptide derived from p16CDKN2/INK4A. Curr Biol 1996;6:84–91.
30. Russo AA, Tong L, Lee JO, Jeffrey PD, Pavletich NP. Structural basis for inhibition of the cyclin-dependent kinase Cdk6 by the tumour suppressor p16INK4a. Nature 1998;395:237–43.
31. Suzuki-Takahashi I, Higashi H, Yoshida E, Nishimura S, Kitagawa M. Effects of exogenous p16INK4a on growth of cells with various status of cell-cycle regulators. Biochem Biophys Res Commun 1997;234:386–92.
32. Tomita T. Cyclin-dependent kinase (cdk6) andh p16 in pancreatic endocrine neoplasms. Pathology 2004;36:566–70.
33. Cho HS, Kelly JD, Hayami S, Toyokawa G, Takawa M, Yoshimatsu M, et al. Enhanced expression of EHMT2 is involved in the proliferation of cancer cells through negative regulation of SIAH1. Neoplasia 2011;13: 676–84.
34. Grossel MJ, Hinds PW. From cell cycle to differentiation: an expanding role for cdk6. Cell Cycle 2006;5:266–70.
35. Hu MG, Deshpande A, Enos M, Mao D, Hinds EA, Hu GF, et al. A requirement for cyclin-dependent kinase 6 in thymocyte development and tumorigenesis. Cancer Res 2009;69:810–8.
36. Mendrzyk F, Radlwimmer B, Joos S, Kokocinski F, Benner A, Stange DE, et al. Genomic and protein expression profiling identifies CDK6 as novel independent prognostic marker in medulloblastoma. J Clin Oncol 2005;23:8853–62.
37. Canepa ET, Scassa ME, Ceruti JM, Marazita MC, Carcagno AL, Sirkin PF, et al. INK4 proteins, a family of mammalian CDK inhibitors with novel biological functions. IUBMB Life 2007;59:419–26.
38. Semenza GL. Regulation of physiological responses to continuous and intermittent hypoxia by hypoxia-inducible factor 1. Exp Physiol 2006;91:803–6.
39. Rhodes DR, Kalyana-Sundaram S, Mahavisno V, Varambally R, Yu J, Briggs BB, et al. Oncomine 3.0: genes, pathways, and networks in a collection of 18,000 cancer gene expression profiles. Neoplasia 2007;9:166–80.
40. Cortez CC, Jones PA. Chromatin, cancer and drug therapies. Mutat Res 2008;647:44–51.
41. Ma WW, Adjei AA. Novel agents on the horizon for cancer therapy. CA Cancer J Clin 2009;59:111–37.
42. Huang Y, Stewart TM, Wu Y, Baylin SB, Marton LJ, Perkins B, et al. Novel oligoamine analogues inhibit lysine-specific demethylase 1 and induce reexpression of epigenetically silenced genes. Clin Cancer Res 2009;15:7217–28.

Cell Metabolism
Article

Crosstalk between Glucocorticoid Receptor and Nutritional Sensor mTOR in Skeletal Muscle

Noriaki Shimizu,[1,10] Noritada Yoshikawa,[1,2,10] Naoki Ito,[3,4] Takako Maruyama,[1] Yuko Suzuki,[3] Sin-ichi Takeda,[3] Jun Nakae,[5] Yusuke Tagata,[9] Shinobu Nishitani,[9] Kenji Takehana,[9] Motoaki Sano,[6] Keiichi Fukuda,[6] Makoto Suematsu,[7,8] Chikao Morimoto,[1,2] and Hirotoshi Tanaka[1,2,*]

[1]Division of Clinical Immunology, Advanced Clinical Research Center
[2]Department of Rheumatology and Allergy, Research Hospital
Institute of Medical Science, University of Tokyo, Tokyo 108-8639, Japan
[3]Department of Molecular Therapy, National Institute of Neuroscience, National Center of Neurology and Psychiatry, Kodaira 187-8502, Japan
[4]Department of Biological Information, Tokyo Institute of Technology, Yokohama 226-8501, Japan
[5]Frontier Medicine on Metabolic Syndrome, Division of Endocrinology, Metabolism and Nephrology, Department of Internal Medicine
[6]Cardiology Division, Department of Internal Medicine
[7]Department of Biochemistry
[8]JST ERATO, Suematsu Gas Biology Project
Keio University School of Medicine, Tokyo 160-8582, Japan
[9]Ajinomoto Pharmaceuticals Co., Ltd., Kawasaki 210-8681, Japan
[10]These authors contributed equally to this work
*Correspondence: hirotnk@ims.u-tokyo.ac.jp
DOI 10.1016/j.cmet.2011.01.001

SUMMARY

Maintenance of skeletal muscle mass relies on the dynamic balance between anabolic and catabolic processes and is important for motility, systemic energy homeostasis, and viability. We identified direct target genes of the glucocorticoid receptor (GR) in skeletal muscle, i.e., REDD1 and KLF15. As well as REDD1, KLF15 inhibits mTOR activity, but via a distinct mechanism involving BCAT2 gene activation. Moreover, KLF15 upregulates the expression of the E3 ubiquitin ligases atrogin-1 and MuRF1 genes and negatively modulates myofiber size. Thus, GR is a liaison involving a variety of downstream molecular cascades toward muscle atrophy. Notably, mTOR activation inhibits GR transcription function and efficiently counteracts the catabolic processes provoked by glucocorticoids. This mutually exclusive crosstalk between GR and mTOR, a highly coordinated interaction between the catabolic hormone signal and the anabolic machinery, may be a rational mechanism for fine-tuning of muscle volume and a potential therapeutic target for muscle wasting.

INTRODUCTION

Muscle comprises ~40% of body mass and contributes not only to the structure and movement of the body but also to nutrient storage and supply (Matthews, 1999). In adult mammals, skeletal muscle hypertrophy/atrophy is characterized by an increase/decrease in the size (as opposed to the number) of individual myofibers, respectively. The control of muscle mass is believed to be determined by a dynamic balance between anabolic and catabolic processes (Hoffman and Nader, 2004). Mammalian target of rapamycin (mTOR) is a crucial component of the anabolic machinery for protein synthesis. mTOR consists of two complexes: mTORC1, which includes Raptor, signals to S6K and 4E-BP1, controls protein synthesis, and is rapamycin sensitive; and mTORC2, which includes Rictor, signals to Akt, and is rapamycin insensitive. mTORC1 integrates four major signals: growth factors, energy status, oxygen, and amino acids, especially branched-chain amino acids (BCAAs). Prototypically, insulin/IGF-1 activates mTOR via the PI3K-Akt pathway (Sengupta et al., 2010). It is currently considered that mTORC1, and not mTORC2, is essential for the maintenance of muscle mass and function (Bentzinger et al., 2008; Risson et al., 2009). Protein degradation in skeletal muscle cells is essentially mediated by the activity of two conserved pathways: the ubiquitin-proteasomal pathway and the autophagic/lysosomal pathway (Sandri, 2008). The ubiquitin-proteasomal pathway is responsible for the turnover of the majority of soluble and myofibrillar muscle proteins. The activity of this pathway is markedly increased in atrophying muscle due to the transcriptional activation of a set of E3 ligase-encoding genes, e.g., atrogin-1 and MuRF1 (Glass, 2003; Sandri et al., 2004). Autophagy also plays an important role in the degradation of skeletal muscle, and is indicated to be a consequence of an ordered transcriptional program involving a battery of genes, e.g., LC3 and Bnip3 (Mizushima et al., 2008). These positive and negative pathways are balanced in a highly coordinated manner for the determination of myofiber size and total muscle volume; however, distortion of this balance with a relative increase in degradation results in the generalized decrease of myofiber size and muscle atrophy (Hoffman and Nader, 2004). Pioneering studies demonstrated that muscle atrophy is a result of active processes that are transcriptionally controlled through the expression of a particular gene set; the forkhead box O (FoxO) transcription factors are

common components of a number of atrophy models and act as critical liaison molecules for protein degradation and autophagy via the transcriptional regulation of, for example, atrogin-1, MuRF1, LC3, and Bnip3 (Mammucari et al., 2007; Sandri et al., 2004; Stitt et al., 2004; Zhao et al., 2007). In clear contrast, it is evident that each disease has proper signaling pathways to FoxOs and that other components of the cellular machinery often participate in the progression of atrophy (Moresi et al., 2010; Suzuki et al., 2007). Therefore, for the development of therapies against muscle atrophy, it should be addressed how the transcriptional program triggered by a particular atrophy pathway is orchestrated and how the balance of muscle protein synthesis and degradation is distorted in each disease.

Adrenal glucocorticoids produce their actions via a signal pathway involving the ubiquitously expressed glucocorticoid receptor (GR), a prototypic member of the nuclear receptor superfamily, which acts as a ligand-dependent transcription factor. Upon binding glucocorticoids, GR translocates into the nucleus and binds to the glucocorticoid response element (GRE) in the promoters of target genes. The binding of liganded receptors to target DNA is followed by the recruitment of mediators and coactivators to the proximity of GRE, resulting in the recruitment of RNA polymerase II (RNAPII) to nearby transcription start sites and the activation of transcription (Evans, 2005; Meijsing et al., 2009). In skeletal muscle, glucocorticoids elicit a variety of biological actions in the metabolism of glucose, lipids, and proteins and contribute to metabolic homeostasis (Munck et al., 1984). On the other hand, the prolonged oversecretion or exogenous administration of glucocorticoid gives rise to undesirable effects including muscle atrophy (Munck et al., 1984). Although many studies addressed the mechanism of glucocorticoid-induced muscle atrophy, how the glucocorticoid-GR system generates the functional coupling between metabolic regulation and volume adjustment in skeletal muscle remains unsolved. Of note, many pathological conditions characterized by muscle atrophy, e.g., sepsis, cachexia, starvation, metabolic acidosis, and severe insulinopenia, are associated with an increase in circulating glucocorticoid levels. Adrenalectomy or treatment with the GR antagonist RU486 attenuates muscle atrophy in sepsis, cachexia, starvation, and severe insulinopenia (Menconi et al., 2007; Schakman et al., 2008). Moreover, endogenous glucocorticoids were shown to be essential for muscle atrophy in acute diabetic rodents (Hu et al., 2009). Together, understanding the glucocorticoid-mediated regulation of metabolism-volume coupling in muscle is increasingly important for the management of not only muscle atrophy but also these wasting/metabolic disorders.

Typically, glucocorticoid-induced muscle atrophy is characterized by fast-twitch type II glycolytic muscle fiber loss with reduced or no impact on type I fibers. The mechanism of such fiber specificity is yet unknown. Previous reports suggested that the glucocorticoid-GR system has antianabolic and catabolic effects and promotes degradation via the induction of a set of genes including atrogin-1, MuRF1, and myostatin (Menconi et al., 2007; Schakman et al., 2008). Although the involvement of FoxO transcription factors is reported in the gene regulation of atrogin-1 and MuRF1 under the presence of excess glucocorticoids (Sandri et al., 2004; Stitt et al., 2004), the biochemical role of GR in the transcriptional regulation of muscle tissue has not yet been determined. Therefore, we investigated how GR-mediated gene expression coordinately modulates antianabolic and catabolic actions to understand the functional coupling of metabolism and volume regulation in muscle.

In the present study, we identified REDD1 and KLF15 genes as direct targets of GR. REDD1 is known to be induced by various stressors, including glucocorticoid, and to inhibit mTOR activity via the sequestration of 14-3-3 and the increase of TSC1/2 activity (Wang et al., 2006; DeYoung et al., 2008). We clearly identified the functional GRE via the promoter analysis of REDD1 gene. On the other hand, KLF15 is a recently discovered transcription factor that is involved in several metabolic processes in skeletal muscle; e.g., KLF15 transcriptionally upregulates the gene expression of branched-chain aminotransferase 2 (BCAT2), a mitochondrial enzyme catalyzing the first reaction in the catabolism of BCAA to accelerate BCAA degradation and alanine production in skeletal muscle (Gray et al., 2007). Moreover, phenotypic analysis of cardiac-specific KLF15 knockout mice revealed marked left ventricular hypertrophy, indicating the negative regulatory role of KLF15 on muscle mass (Fisch et al., 2007). We here demonstrated that KLF15 participates in muscle catabolism via the transcriptional regulation of atrogin-1 and MuRF1. Moreover, KLF15 affects mTOR through BCAA degradation and negatively modulates myofiber size. mTOR activation inhibits GR-mediated transcription by suppressing GR recruitment onto target genes, strongly suggesting a mutually exclusive crosstalk between mTOR and GR. Pharmacological activation of mTOR with BCAA attenuated GR-mediated gene expression, leading to the substantial restoration of muscle in glucocorticoid-treated rats. We, therefore, indicate the critical importance of the interaction of GR and mTOR in the regulation of metabolism-volume coupling in skeletal muscle.

RESULTS

REDD1 and KLF15 Are Target Genes of GR in Skeletal Muscle

GR levels were relatively high in type II-rich gastrocnemius and tibialis anterior muscles compared to type I-rich soleus muscle in rats (Figure 1A). Figure 1B illustrates the comparison of the effects of a 3 hr treatment with dexamethasone (DEX) on mRNA expression of various genes between the gastrocnemius and soleus muscles. Hormonal induction of mRNA expression of REDD1, atrogin-1, MuRF1, KLF15, FoxO1, FoxO3, and myostatin, as well as the well-known GR target gene FKBP5 (Yoshikawa et al., 2009), was observed in both muscles, but to a lesser extent in the soleus muscle. Among the genes induced by DEX at 3 hr (Figure 1B), the promoter regions of MuRF1 (Waddell et al., 2008) and myostatin (Ma et al., 2001), but not atrogin-1 (Sandri et al., 2004), contain functional GREs. In addition, REDD1 and KLF15 were also considered as candidates of GR target genes (see the Supplemental Information available online).

Concerning KLF15, we showed, in gastrocnemius muscle and L6 myotubes but not in liver, that KLF15 mRNA and protein expression was induced in a GR-dependent manner (Figure 2A). The promoter region spanning from −4676 to +116 of KLF15 gene was not responsive to DEX; however, the activity of the region spanning −2108 to +1331 was induced by DEX, and

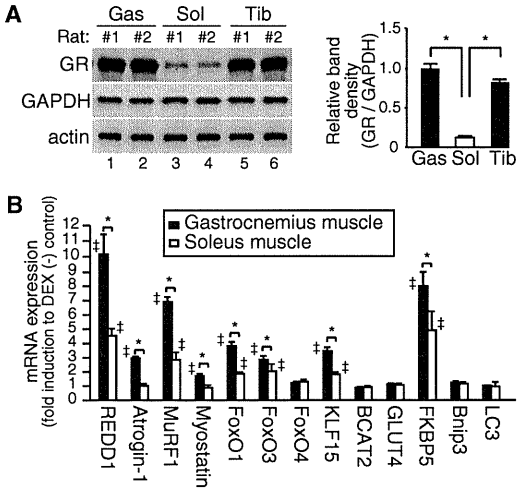

Figure 1. GR Protein Expression and Glucocorticoid-Dependent mRNA Expression of Atrophy-Related Genes in Rat Skeletal Muscles

(A) GR protein levels in rat gastrocnemius (Gas), soleus (Sol), and tibialis anterior (Tib). Left, representative immunoblots. Right, quantified protein levels of GR relative to GAPDH (n = 9).

(B) Induction of mRNA levels of atrophy-related genes by dexamethasone (DEX). Expression levels of the indicated mRNA in the muscles from rats 3 hr after intraperitoneal injection with DEX were assessed in quantitative RT-PCR (qRT-PCR). Results are shown as fold induction to vehicle-treated rats (n = 6).

(A and B) Error bars show SD. $^{*}p < 0.05$, $^{\dagger}p < 0.05$ versus vehicle-treated rats.

this induction was inhibited by a GR antagonist RU486. The deletion and mutational analyses of KLF15 promoter indicated that both upper GRE1 and lower GRE2 sites were functional (Figures 2B and 2C). The transient transfection assays using the reporter constructs conveying these minimal GRE sites clearly showed that each GRE is independently functional (Figure 2D). A chromatin immunoprecipitation (ChIP) assay revealed that both GRE-like sequences were targeted by GR and that RNAPII was incorporated onto the coding region of KLF15 gene in the presence of DEX in L6 cells (Figure 2E). We also confirmed the DEX-dependent recruitment of endogenous GR onto the KLF15 promoter in a skeletal muscle-specific manner in vivo (Figure 2F). Similarly, we identified the functional GRE on the REDD1 promoter region and confirmed REDD1 as a GR target gene as well (Figure S1).

KLF15 Transactivates atrogin-1 and MuRF1 Genes

Next, we studied the alteration in the gene expression profile after the direct injection of a KLF15-expressing adenovirus into the rat tibialis anterior muscle. The exogenous expression of KLF15 increased KLF15 protein levels by approximately 5-fold (Figure 3A) and significantly induced mRNA expression of its target gene BCAT2 as anticipated (Figure 3B). Moreover, mRNA expression of atrogin-1, MuRF1, FoxO1, and FoxO3 was stimulated by KLF15 (Figure 3B). We then focused on atrogin-1 and MuRF1 and asked whether the DEX-mediated induction of their mRNA expression was dependent on KLF15. For that purpose, we tested the effect of knocking down the expression of GR or KLF15 on mRNA expression of KLF15, atrogin-1, and MuRF1 as well as another GR target gene REDD1 as a control. In L6 myoblasts, GR knockdown diminished the DEX-dependent mRNA induction of all of these GR target genes. However, KLF15 knockdown affected that of atrogin-1 and MuRF1 but not REDD1 (Figure 3C). These results strongly indicate the critical involvement of the GR-KLF15 cascade in the DEX-mediated upregulation of atrogin-1 and MuRF1 gene expression. To address the role of KLF15 in the transcriptional regulation of atrogin-1 and MuRF1, we constructed luciferase reporter plasmids driven by the promoter of rat atrogin-1 or MuRF1, and tested the effect of the exogenous expression of KLF15 in L6 myoblasts. The expression of the reporter genes was upregulated in a KLF15-dependent manner (Figure 3D). Since the promoter regions of atrogin-1 and MuRF1 contain a number of putative KLF15 recognition sites, we performed ChIP analyses; both promoters had multiple KLF15 binding sites and some of them were located in the proximity of FoxO binding sites and GRE (Figure 3E), and at least one of these KLF15 sites of each promoter recruited KLF15 in a DEX-dependent manner in vivo as well (Figure 3F). Note that atrogin-1 and MuRF1 were originally identified as FoxO target genes (Sandri et al., 2004; Waddell et al., 2008) and that KLF15 induced FoxO mRNA expression (Figure 3B). Indeed, the combination of KLF15 and FoxO significantly enhanced the promoter activity of atrogin-1 and MuRF1 when compared to their individual effects (Figure 3G). Moreover, the direct injection of the adenovirus expressing constitutively active FoxO1 or KLF15 significantly increased atrogin-1 and MuRF1 mRNA expression, and the expression of both resulted in synergistic or additive effects in tibialis anterior (Figure 3H). Therefore, it is likely that KLF15 and FoxO transcription factors cooperatively upregulate the expression of atrogin-1 and MuRF1 genes.

GR-KLF15 Axis Modulates BCAA Metabolism and mTOR Activity

Next, we studied the effects of glucocorticoids, GR, and KLF15 on BCAT2 and BCAA catabolism in skeletal muscle cells. In gastrocnemius muscle, mRNA expression of KLF15 preceded that of BCAT2 after treatment with DEX (Figure 4A). Overexpression of KLF15 increased the BCAT2 promoter-luciferase reporter activity (Figure 4B). Moreover, DEX-induced BCAT2 promoter activation was inhibited by either RU486 or siKLF15 (Figure 4C), indicating that KLF15 is mandatory for GR-mediated BCAT2 gene activation. BCAT2 enzyme activity was stimulated by DEX, and this effect was abolished in the presence of RU486 (Figure 4D). In tibialis anterior muscle and L6 myotubes, the adenovirus-mediated exogenous expression of KLF15 significantly induced BCAT2 enzyme activity even in the absence of DEX (Figure 4E).

The measurement of intracellular amino acid levels clearly revealed the accelerated catabolism of BCAA by KLF15 in myotubes; the exogenous expression of KLF15 decreased the levels of Val, Leu, and Ile, with a reciprocal increase in Ala and Glu without significant alterations in, for example, Gly, Trp, Gln, Tyr, and Phe, in L6 myotubes (Figure 4F). Amino acids, especially BCAA, are believed to activate mTOR and to increase in association with Rheb-mTOR (Sancak et al., 2010). We showed that overexpression of KLF15 in C2C12 myotubes suppressed mTOR activity as demonstrated by the decrease in the phosphorylated form of S6K1. Moreover, mTOR activity was complemented by the addition of excess BCAA (Figure 4G). Of note,

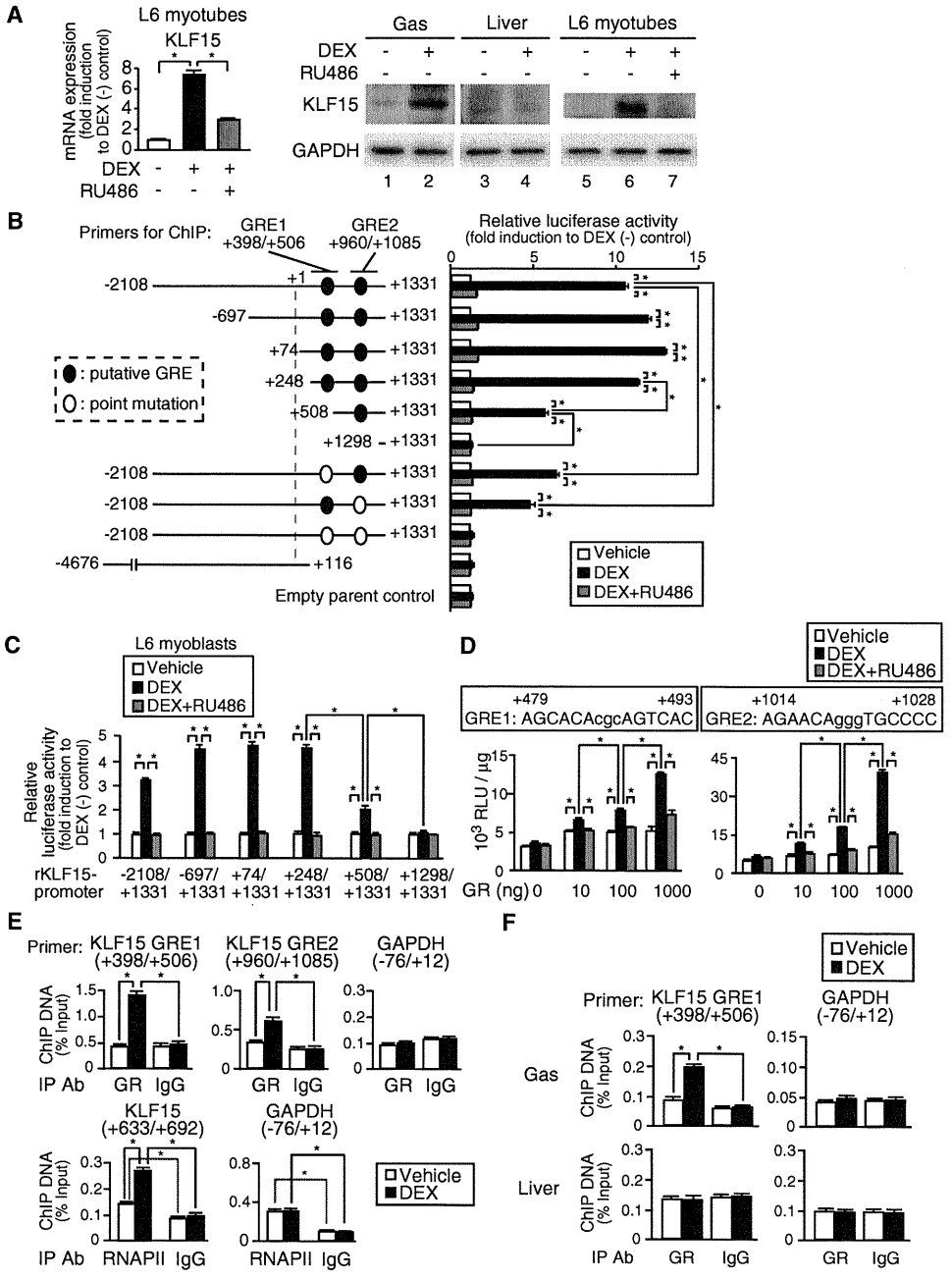

Figure 2. Identification of KLF15 as a Direct GR Target Gene

(A) GR-dependent mRNA (left) and protein (right) expression of KLF15 in L6 myotubes treated with DEX and RU486 for 6 hr and in DEX-treated rat gastrocnemius (see legend for Figure 1B).

(B) Identification of GREs in rat KLF15 promoter. Left, schematic of rat KLF15 promoter-luciferase reporter constructs. Positions of the primers for chromatin immunoprecipitation (ChIP) in (E) and (F) are shown. Right, GR-dependent activation of rat KLF15 promoter-reporter genes. COS-7 cells were transfected with the reporter constructs and 100 ng of GR expression plasmid and treated with DEX and RU486 for 18 hr.

(C) GR-dependent activation of rat KLF15 promoter-reporter genes in L6 myoblasts treated with DEX and RU486 for 18 hr.

(D) GR-dependent activation of reporter genes containing KLF15 promoter GREs. L6 myoblasts were transfected with the luciferase reporter constructs containing the GREs from rat KLF15 with GR expression plasmid and treated with DEX and RU486 for 18 hr.

(E) DEX-dependent recruitment of GR and RNAPII onto rat KLF15 gene. L6 myotubes treated with 1 µM DEX for 2 hr were subjected to ChIP.

(F) Skeletal muscle-specific recruitment of GR onto rat KLF15 gene by DEX. DEX-treated rat gastrocnemius (Gas) and liver (see legend for Figure 1B) were subjected to ChIP.

(A–F) Error bars show SD (n = 5). *p < 0.05.

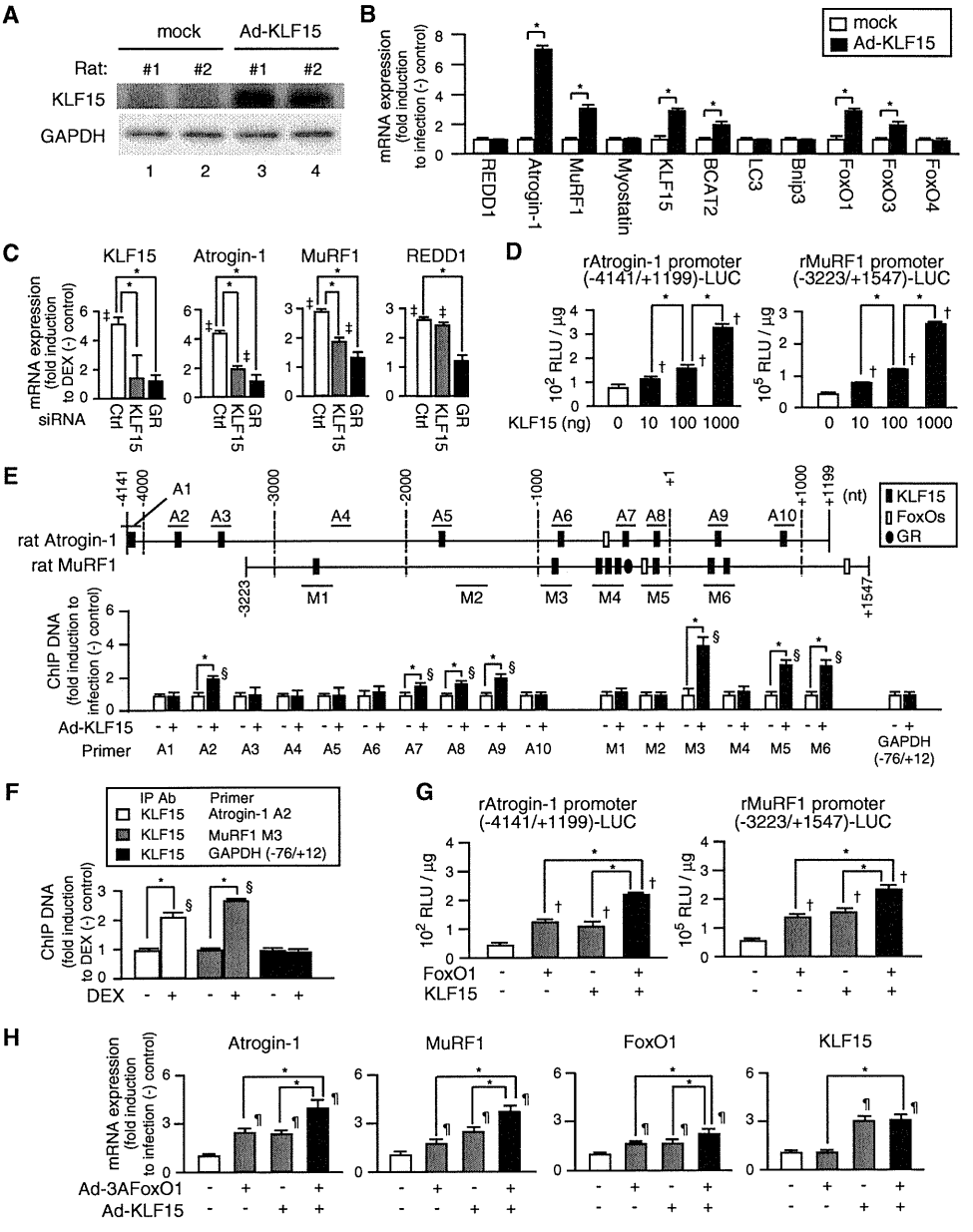

Figure 3. Transcriptional Regulation of Atrogenes by KLF15 and FoxOs

(A and B) KLF15-dependent mRNA expression of atrophy-related genes. Recombinant adenovirus Ad-KLF15 was infected to rat tibialis anterior for 7 days. (A) Immunoblot detection of ectopic KLF15. (B) qRT-PCR.

(C) Effects of knockdown of KLF15 or GR on DEX-dependent mRNA expression of atrophy-related genes. L6 myoblasts were transfected with control siRNA, siRNA against KLF15, or siRNA against GR and treated with DEX for 18 hr.

(D) KLF15-dependent activation of rat atrogin-1 (left) and MuRF1 (right) promoter-reporter genes in L6 myoblasts.

(E) Mapping of the binding sites for KLF15, FoxOs, and GR in rat atrogin-1 and MuRF1 promoters. Top, putative binding sites identified in in silico promoter analysis (see the Experimental Procedures and the Supplemental Information). Bars indicate the positions of the primers for ChIP. Bottom, recruitment of KLF15 onto rat atrogin-1 and MuRF1 promoters. L6 myotubes were infected with Ad-KLF15 for 5 days and subjected to ChIP using anti-KLF15 antibody.

(F) DEX-dependent recruitment of KLF15 onto rat atrogin-1 and MuRF1 promoters in rat gastrocnemius (see Figure 1B).

(G and H) Effects of FoxOs and KLF15 on rat atrogin-1 and MuRF1 promoter-reporter gene expression in L6 myoblasts (G) and on atrogin-1 and MuRF1 mRNA expression in rat tibialis anterior (H). (G) Luciferase assay of L6 myoblasts transfected with the reporter constructs with or without FoxO1 and/or KLF15 expression plasmids. (H) qRT-PCR analysis of rat tibialis anterior expressing ectopic KLF15 and/or constitutive active FoxO1 (3AFoxO1) for 3 days.

(B–H) Error bars show SD (n = 5). *$p < 0.05$, ‡$p < 0.05$ versus vehicle-treated cells, †$p < 0.05$ versus mock-transfected cells, §$p < 0.05$ versus ChIP with normal IgG, ¶$p < 0.05$ versus mock-infected rats.

the diameter of C2C12 myotubes was shortened by KLF15 and rescued by BCAA (Figure 4G). Moreover, exogenous KLF15 reduced mTOR activity with fiber type-independent atrophy in the tibialis anterior muscle (Figure 4H). Taken together, these data indicate that KLF15 is a liaison molecule for GR in the induction of atrogenes and the acceleration of BCAA catabolism and mTOR repression to decrease myofiber size.

mTOR Affects GR-Mediated Transcriptional Regulation

Since little is known about how glucocorticoid-mediated catabolic signal transduction is shut off, we next examined the effects of mTOR blockade using rapamycin on GR-mediated gene expression in L6 myotubes. Surprisingly, rapamycin significantly enhanced the DEX-induced mRNA expression of a number of GR target genes, including REDD1, atrogin-1, MuRF1, KLF15, FoxOs, and FKBP5 (Figure 5A). These results strongly suggest that mTOR blockade selectively enhances mRNA expression of GR target genes, i.e., mTOR activation appears to have a negative impact on GR-mediated gene expression. To further address this negative modulation of GR function by mTOR, we performed transient transfection assays using GR-responsive KLF15 promoter-Luc and GRE-Luc reporter genes in L6 myoblasts. A constitutively active mutant of Rheb, RhebS16H, which autonomously activates mTOR, repressed DEX-mediated reporter gene activation, and rapamycin inhibited these negative effects of RhebS16H (Figure 5B). Moreover, a major endogenous mTOR activator IGF-1 slightly enhanced S6K1 phosphorylation and did not affect DEX-induced GRE-Luc expression when cultured in amino acid-rich media. In clear contrast, in amino acid-deprived media, DEX-dependent induction of GRE-Luc was approximately doubled, and IGF-1 strongly phosphorylated S6K1 and suppressed DEX-induced GRE-Luc expression (Figure 5C). These results indicated that, regardless of the upstream pathways for mTOR activation, endogenous GR activity is negatively controlled by mTOR in L6 myoblasts.

We then asked the underlying mechanisms for mTOR-mediated GR suppression. To test whether mTOR-mediated GR repression is via global protein synthesis downstream of mTOR, we examined luciferase mRNA expression in transient transfection assay using GRE-Luc reporter plasmid in the presence or absence of the protein synthesis inhibitor cycloheximide. Cycloheximide did not influence on either GR-mediated GRE activation or BCAA-mediated GR suppression (Figure 5D). Therefore, BCAA inhibits the transcriptional effects of GR via mTOR activation but not via de novo protein synthesis. Immunoblotting using L6 myotubes revealed that GR protein levels were unaltered in the presence of DEX, BCAA, or rapamycin. Treatment with DEX clearly promoted the nuclear translocation of GR, and such a process was not affected by BCAA or rapamycin (Figure 5E). Concerning the promoter regions spanning the putative GREs in KLF15 and REDD1, DEX-induced GR recruitment was significantly enhanced by rapamycin, suggesting that mTOR negatively influences the access of GR to these promoters. Such an enhancement of GR promoter binding by rapamycin was paralleled by RNAPII recruitment onto the coding regions of KLF15 and REDD1 (Figure 5F). Thus, cellular mTOR activity negatively modulates GR transcriptional function, most possibly by altering the intranuclear behavior of GR. We finally examined the effect of constitutive mTOR activation by studying the impact of adeno-associated virus-driven RhebS16H expression on S6K1 activity and the gene expression profile of the tibialis anterior muscle from DEX-treated rats. RhebS16H-injected muscle had elevated levels of S6K1 phosphorylation and significant decreases in the induction response to DEX of a number of glucocorticoid-inducible genes, including REDD1, atrogin-1, MuRF1, FoxOs, KLF15, and FKBP5, when compared to mock-injected muscle (Figures 5G and 5H).

mTOR Activation Attenuates Glucocorticoid-Induced Muscle Atrophy

It should be noted that numerous studies examined the effects of BCAA on mTOR activity in glucocorticoid-induced atrophy models with conflicting results, the reason for which might be variations in the protocols used in those in vivo studies (Menconi et al., 2007; Schakman et al., 2008). We showed that the bolus administration of a BCAA cocktail via a gastric tube just before the peritoneal injection of DEX (Supplemental Information) resulted in sufficient and reproducible mTOR activation in the gastrocnemius muscle; the phosphorylated form of S6K1 was increased at 30 min after BCAA administration and returned to the baseline level after 90–180 min, even in the presence of DEX (Figure 6A). We then tested the effects of DEX, BCAA, and rapamycin on the protein levels and phosphorylation status of mTOR and its downstream effectors S6K1 and 4E-BP1 as well as Akt, the upstream activator of mTOR, in the rat glucocorticoid-induced atrophy model (5 day intraperitoneal DEX administration, see the Supplemental Information). In GR-rich gastrocnemius muscle, treatment with DEX suppressed the phosphorylation of S6K1 and 4E-BP1, without a significant alteration in p-Akt, indicating that DEX inhibited mTOR function in an Akt-independent fashion in this model. In clear contrast, in either the soleus muscle or liver, DEX treatment did not affect mTOR activity. When BCAA was supplemented, the levels of p-S6K1 and p-4E-BP1 were efficiently restored. Of note, rapamycin canceled these effects of BCAA (Figure 6B). In this model, BCAA administration suppressed the glucocorticoid-induced expression of REDD1, atrogin-1, MuRF1, KLF15, FoxOs, and FKBP5 mRNA (Figure 6C), and there was a decrease in GR recruitment onto the promoters of KLF15, REDD1, MuRF1, and FKBP5 (Figure 6D). BCAA administration also repressed the expression of BCAT2, GLUT4, Bnip3, and LC3 mRNA, and treatment with rapamycin inhibited the effects of BCAA (Figure 6C). In contrast, in the soleus muscle, treatment with DEX alone or DEX plus BCAA only marginally influenced mTOR activity and the gene expression profile, if at all (Figures 6B and 6C).

In this glucocorticoid-induced muscle atrophy rat model, there was a decrease in the body weight of the DEX, DEX plus BCAA, and DEX plus BCAA plus rapamycin groups (Figure 7A). The DEX plus BCAA group revealed a significant restoration of muscle strength as determined by a grip test and the weight of the gastrocnemius muscle when compared with DEX group (Figures 7B and 7C). Histological examination of the gastrocnemius muscle demonstrated typical type II fiber-dominant atrophy in the DEX group; however, the DEX plus BCAA group showed less impairment in the gastrocnemius muscle that was represented by the prevention of type II fiber loss. Semiquantitative analysis using cross-sectional area (CSA) analysis of myofibers strongly supported this notion; the leftward shift in myofiber size

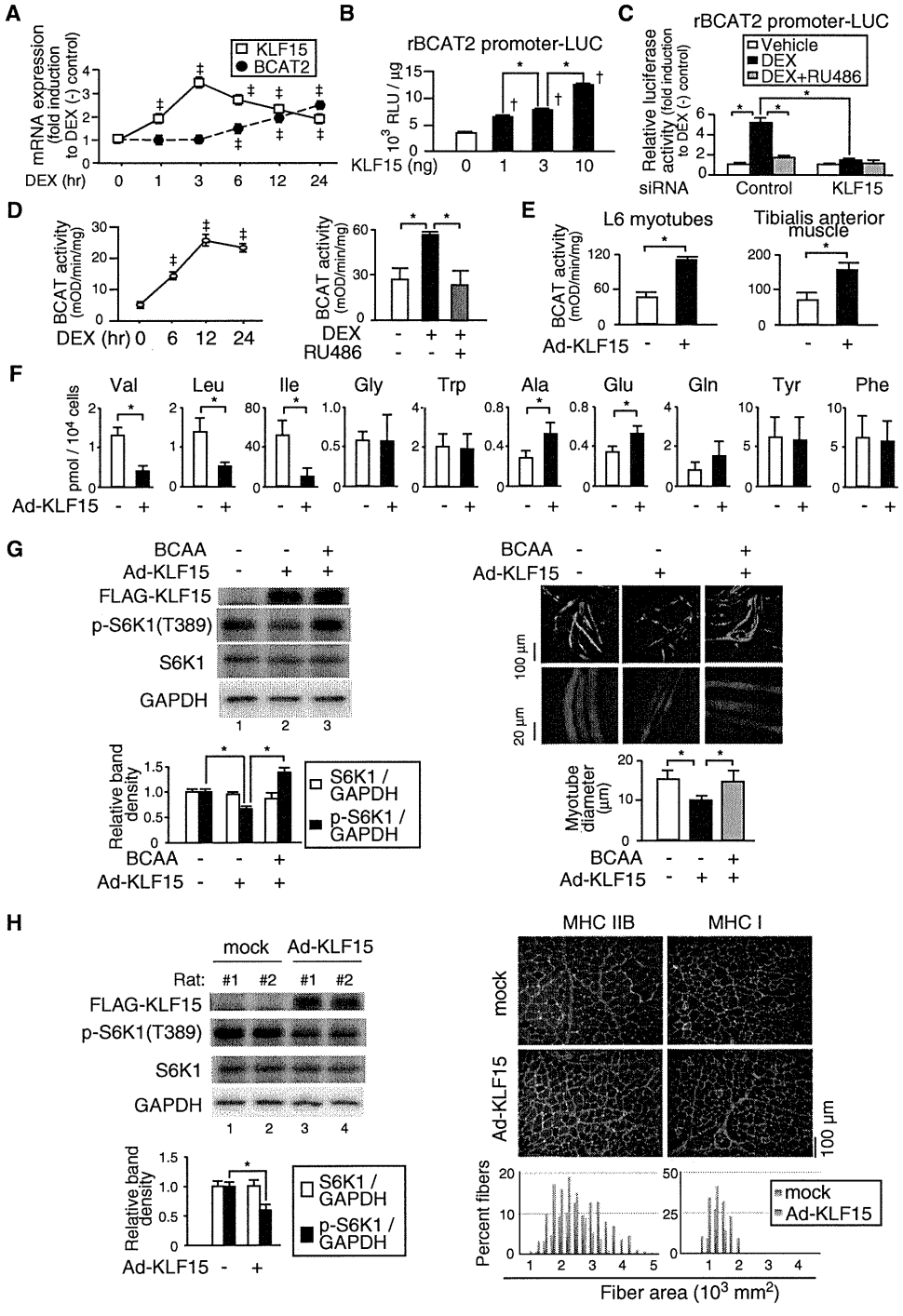

Figure 4. KLF15-Mediated Modulation of BCAA Metabolism and Myofiber Size

(A) Time course of mRNA expression of KLF15 and BCAT2 in rat gastrocnemius after intraperitoneal DEX-injection (n = 5).

(B) KLF15-dependent activation of rat BCAT2 promoter-reporter gene expression in L6 myoblasts (n = 5).

(C) Diminished GR-dependent activation of rat BCAT2 promoter-reporter gene by knockdown of KLF15 in L6 myoblasts (n = 5).

(D) GR-dependent activation of BCAT activity in rat gastrocnemius. Rats were treated with RU486 and/or DEX for the indicated time periods (left) or 6 hr (right) and subjected to BCAT activity measurement as described in the Supplemental Information (n = 5).

(E) KLF15-dependent activation of BCAT activity (n = 5).

(F) Effects of ectopic KLF15 on intracellular amino acid concentrations. L6 myotubes were infected with Ad-KLF15 for 2 days, cultured in amino acid-deprived DMEM for 24 hr, and subjected to quantification of intracellular amino acids as described in the Supplemental Information (n = 3).

(G) Effects of KLF15 and BCAA on mTOR activity and myotube diameter. C2C12 myotubes were infected with GFP-expressing adenovirus and Ad-KLF15 for 2 days and further cultured in amino acid-deprived DMEM supplemented with or without 10 mM BCAA cocktail for 24 hr. Left, representative immunoblots

was observed in the DEX group, but not in the DEX plus BCAA group. In contrast, there was no significant difference in the size of slow type I fibers among the three treatment groups. Moreover, the therapeutic effects of BCAA were inhibited by rapamycin (Figures 7B–7E). Therefore, we conclude that the administration of BCAA elicits mTOR activation and intervenes in GR-dependent catabolic transcriptional regulation to ameliorate DEX-induced muscle atrophy.

DISCUSSION

In skeletal muscle, we suggested that GR activates a secondary transcription network driven by KLF15; that the promoter regions of atrogin-1 and MuRF1 contain KLF15 binding sites as well as those of FoxOs; and that KLF15 induces the expression of these atrogenes. Although the molecular mechanism remains elusive, the functional cooperativity of GR, FoxOs, and KLF15 in the expression of the atrogenes may represent the molecular basis for the involvement of GR in muscle atrophy associated with a number of pathological conditions including diabetes and sepsis. From the metabolic viewpoint, these GR-driven transcriptional cascades appear to be relevant for providing rapid and integrated cues toward muscle breakdown and nutrient supply from muscle to other organs, i.e., to the liver, under stressful conditions associated with excess levels of glucocorticoids.

BCAT2 catalyzes the initial step for BCAA degradation, and BCAT2 activity is a critical determinant of cellular BCAA content in skeletal muscle; mice with systemic inactivation of BCAT2 gene are reported to have approximately ten times or higher concentrations of plasma BCAA (She et al., 2007). We demonstrated that BCAA content was decreased with a reciprocal increase in alanine levels in L6 myotubes after the exogenous expression of KLF15 (Figure 4F). Although it is generally known that BCAA is supplied via protein breakdown during skeletal muscle atrophy (Wagenmakers, 1998; Yu et al., 2010), it was reported that net increase in muscle BCAA concentrations after glucocorticoid treatment (~150% increase compared to control) were strikingly lower than those of diabetic rats (~400% increase compared to control) (Aftring et al., 1988; Hundal et al., 1991). This difference in BCAA concentrations is most likely to be due to increased BCAT2 activity in glucocorticoid-treated rats. The glucocorticoid-driven GR-KLF15-BCAT2 axis may negatively modulate the intracellular availability of BCAA and result in a negative impact on mTOR function in skeletal muscle. Indeed, exogenous KLF15 increased mRNA expression of the atrogenes and BCAT2 and decreased mTOR activity and BCAA concentrations in cultured myotubes (Figures 4E–4G). Moreover, the introduction of KLF15 decreased myofiber size in cultured myotubes and caused atrophy in the tibialis anterior muscle, even in the absence of glucocorticoids (Figures 4G and 4H). Therefore, we may conclude that KLF15 is a crucial GR target gene acting as a catabolic modulator of skeletal muscle.

In addition to the KLF15-BCAT2 axis, it should be noted that a number of glucocorticoid-induced products can repress mTOR activity in skeletal muscle cells. Among others, myostatin (Ma et al., 2001; Gilson et al., 2007) and REDD1 (Figure S1) (DeYoung et al., 2008) are direct targets of GR. Moreover, atrogin-1 was recently reported to inhibit S6K1 activity via eIF3f (Csibi et al., 2010). Therefore, it is likely that the mTOR system is negatively regulated by a variety of factors in the presence of excess glucocorticoids in a distinct fashion. Given that the glucocorticoid-GR axis is a major catabolic regulator for homeostatic control (Munck et al., 1984), this multimodal repression of mTOR via the GR axis appears to be rational. In any case, this type of negative mTOR modulation is not reported in other types of muscle atrophy, and may be a striking feature in glucocorticoid-induced muscle atrophy. Interestingly, muscle-specific inactivation of mTOR was reported to exacerbate the myopathic features of type I and type II fiber-rich muscles in a distinct fashion; type I fiber-rich muscles showed prominent dystrophic features with less impact on muscle mass and CSA compared to type II fiber-rich muscles, and a decrease in muscle mass and CSA are characteristic of type II fiber-rich muscles with less dystrophic appearance (Bentzinger et al., 2008; Risson et al., 2009). Therefore, we speculate that type II fiber-rich glycolytic muscles have an evolutionally preserved role for the storage of nutrients under the control of the glucocorticoid-GR axis and that the GR-triggered gene expression program is a purposeful and efficient compensatory mechanism for nutrient supply from those muscles.

An important question is how the GR-driven proteolytic cascades can be shut down when necessary in skeletal muscle. We clearly demonstrated that mTOR activation negatively modulated GR-mediated transcription. Given that the effect of mTOR is rapamycin sensitive, the involvement of mTORC1 is strongly indicated in this interaction. The role of the mTOR pathway in the determination of glucocorticoid sensitivity has not yet been highlighted, except in certain hematologic malignancies (Beesley et al., 2009; Gu et al., 2008; Yan et al., 2006a). It was postulated that the treatment of cultured cells with FK506 or rapamycin enhances glucocorticoid-inducible reporter gene expression, most possibly via their interaction with heat shock proteins and the promotion of the ligand-dependent nuclear entry of GR (Ning and Sanchez, 1993). In contrast, we documented that rapamycin, without any alteration in the cytoplasmic-nuclear distribution of GR, increased GR recruitment onto the promoter (Figures 5E and 5F), and these effects were not reproduced by FK506 (data not shown).

and quantified band densities of S6K1 and p-S6K1(T389) relative to GAPDH (n = 5). Right, representative fluorescent microscopic images of the myotubes and quantified diameters of the myotubes (500 < n < 510).

(H) Effects of ectopic KLF15 expression on mTOR activity and myofiber cross-sectional area (CSA) in rat tibialis anterior. Left, representative immunoblots and quantified band densities (n = 5). Right, immunostaining for type IIB myosin heavy chain (MHC IIB, red in left photographs), type I myosin heavy chain (MHC I, red in right photographs), and type IV collagen (green) of transverse cryosections. CSA distribution of MHC IIB fibers (left) and MHC I fibers (right) are presented as frequency histograms (500 < n < 510).

(A–H) Error bars show SD. *$p < 0.05$, †$p < 0.05$ versus vehicle-treated rats. ‡$p < 0.05$ versus mock-transfected cells.

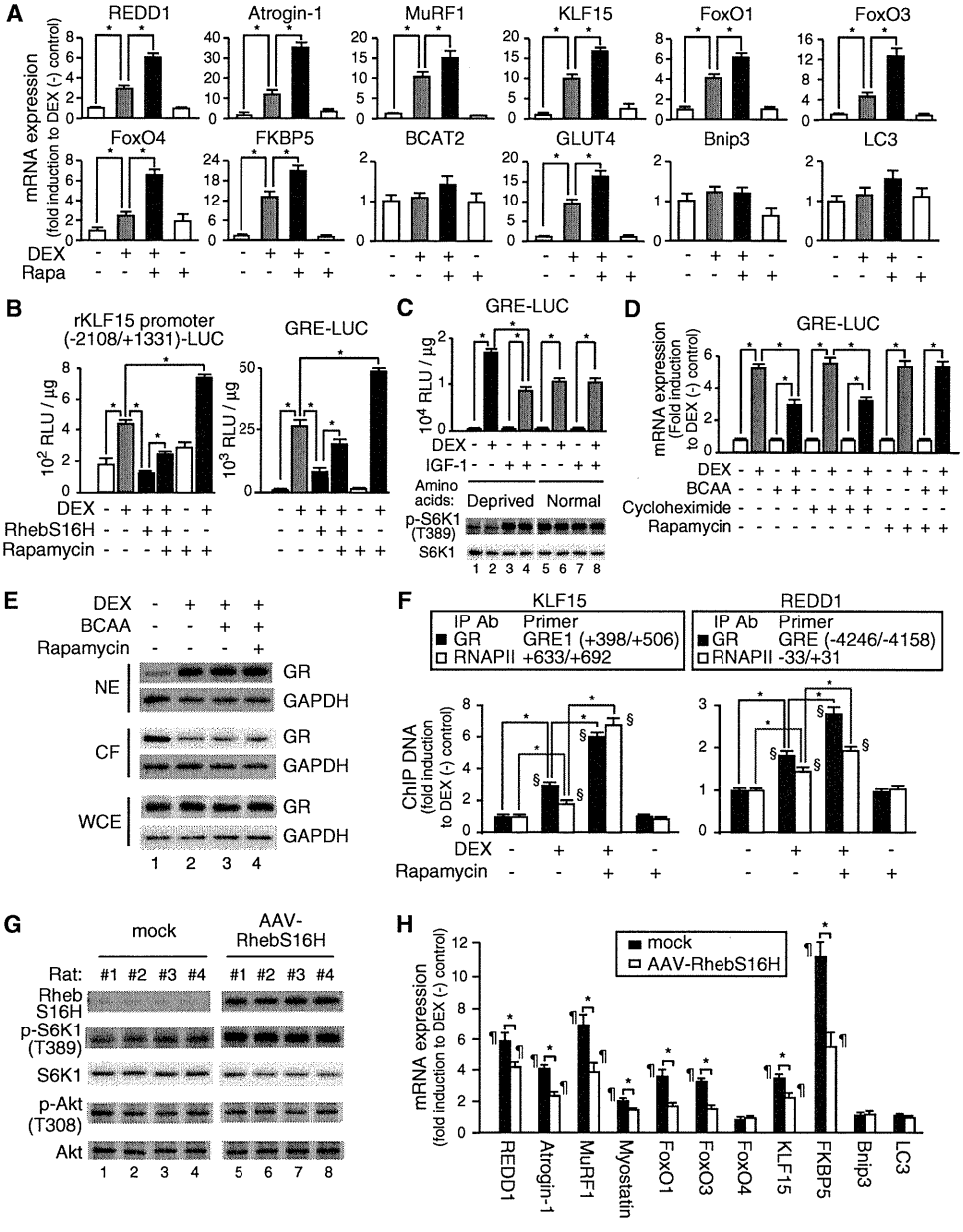

Figure 5. Negative Regulation of GR-Mediated Transcription by mTOR

(A) qRT-PCR analysis of L6 myotubes treated with DEX and rapamycin (Rapa) for 24 hr.

(B) Attenuation of GR-dependent reporter gene expression by mTOR. L6 myoblasts were transfected with rKLF15 promoter-LUC or GRE-LUC, with or without the expression plasmid for a constitutive active Rheb (RhebS16H), and treated with DEX and rapamycin for 18 hr.

(C) Effects of IGF-1 on mTOR activity and GR-dependent reporter gene expression. L6 myoblasts were transfected with GRE-LUC and cultured in amino acid-deprived DMEM (lanes 1–4) or normal DMEM (lanes 5–8) in the presence or absence of IGF-1 and/or DEX for 9 hr. Top, luciferase activities. Bottom, representative immunoblots.

(D) Effects of DEX, BCAA, cycloheximide, and rapamycin on GR-dependent reporter gene expression. L6 myoblasts were transfected with GRE-LUC and cultured in amino acid-deprived DMEM in the presence or absence of 10 mM BCAA cocktail, cycloheximide, rapamycin, and DEX for 6 hr.

(E) Effects of DEX, BCAA, and rapamycin on protein levels and subcellular localization of GR. L6 myotubes were cultured in amino acid-deprived DMEM in the presence or absence of DEX, 10 mM BCAA cocktail, and rapamycin for 30 min. Representative immunoblots of the nuclear extracts (NE), cytoplasmic fractions (CF), and whole-cell extracts (WCE) are shown (n = 3).

(F) Effects of rapamycin on DEX-dependent recruitment of GR onto target gene promoters. L6 myotubes were treated with 1 μM DEX and rapamycin for 2 hr (for KLF15) or 20 min (for REDD1) and processed for ChIP assays.

(G and H) Effects of ectopic expression of RhebS16H on mTOR activity and DEX-mediated mRNA expression. AAV-RhebS16H was infected to rat tibialis anterior for 7 days. (G) Representative immunoblots (n = 7). (H) qRT-PCR analysis of the muscles from the rats 6 hr after intraperitoneal injection with DEX.

(A–D, F, and H) Error bars show SD (n = 5). *$p < 0.05$, §$p < 0.05$ versus ChIP with normal IgG, ¶$p < 0.05$ versus vehicle-treated rats.

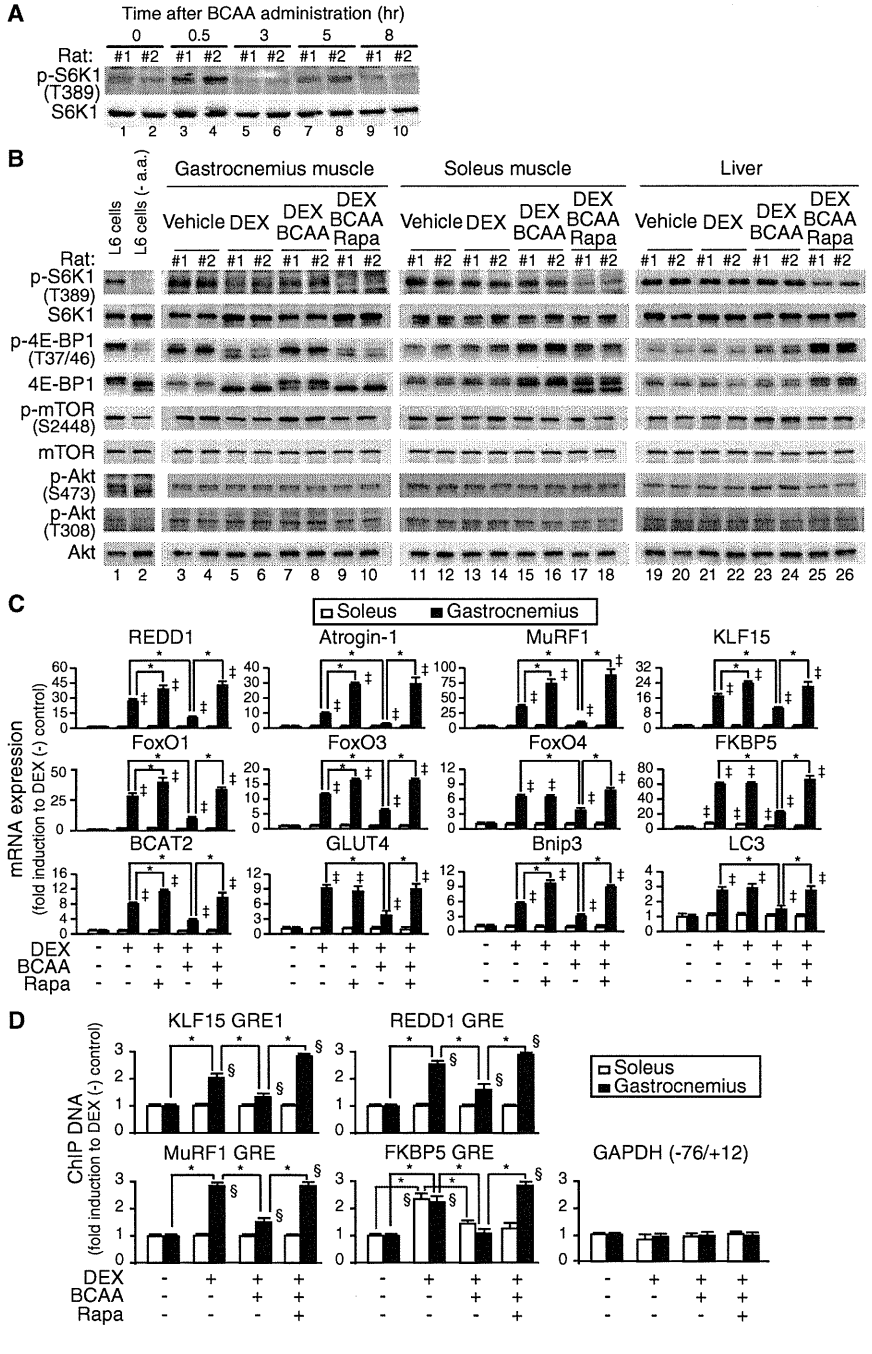

Figure 6. In Vivo Activation of mTOR and Attenuation of GR-Mediated Transcription after Programmed Administration of BCAA

(A) Time course of mTOR activity in rat gastrocnemius after BCAA administration. Representative immunoblots are shown (n = 5).

(B–D) Effects of DEX, BCAA, and rapamycin on mTOR activity; mRNA expression of atrophy-related genes; and GR recruitment onto the target gene promoters. Rats were treated with DEX, BCAA cocktail, and rapamycin for 5 days as described in the Supplemental Information. (B) Representative immunoblots (n = 17). L6 myotubes cultured in normal DMEM and in amino acid-deprived DMEM (–a.a.) for 1 hr were served as controls. (C) mRNA expression of atrophy-related genes. (D) Recruitment of GR onto its target genes. ChIP was performed using anti-GR antibody.

(C and D) Error bars show SD (n = 17). *$p < 0.05$, †$p < 0.05$ versus vehicle-treated rats, §$p < 0.05$ versus ChIP with normal IgG.

In skeletal muscle, this nutrition sensor-driven inhibition of GR function may be one of the mechanisms by which nutrients modulate the internal cellular milieu. Intriguingly, GR-mediated transcription was not repressed by insulin/IGF-1 under normal culture conditions, but did so when amino acids were deprived from the culture media (Figure 5C). This indicates that mTOR may be constitutively activated to a certain extent by nutrients and growth factors to protect cells from GR-driven catabolism in skeletal muscle. Under fasting conditions, however, blood concentrations of insulin/IGF-1 are low, and glucocorticoids may be allowed to efficiently drive the catabolic atrophy program for nutrient supply. Thus, our hypothesis may provide an insight into how muscle cells critically determine their volume after sensing endocrine hormones and the nutritional conditions for homeostatic regulation. In this context, GR-mTOR crosstalk might be a key for creating an interdisciplinary research area that bridges nutrition and medicine.

Therefore, the mTOR-mediated inhibition of GR in skeletal muscle is likely to be due not to the modulation of its chaperone activity but to its intervention in the access of GR to target DNA. It is becoming apparent that mTOR is intimately involved with the transcriptional apparatus in concert with a variety of transcription factors and cofactors (Cunningham et al., 2007). Since mTOR is reported to dock in the nucleus in association with, for example, PML (Bernardi et al., 2006), it would be of particular interest to identify such a factor that tethers GR and mTOR in the nucleus.

The biochemical rationale for the usage of BCAA as a therapeutic tool in glucocorticoid-induced muscle atrophy is that BCAA increases the association between Rheb and mTOR and, at least in part, mimics the effect of Rheb overexpression (Sancak et al., 2010). In our model, BCAA administration repressed mRNA expression of almost all GR-regulated genes (Figure 6C). ChIP analysis strongly supported the notion that BCAA administration inhibited GR recruitment onto the promoters of its target genes (Figure 6D). Moreover, these effects of BCAA were efficiently counteracted by rapamycin.

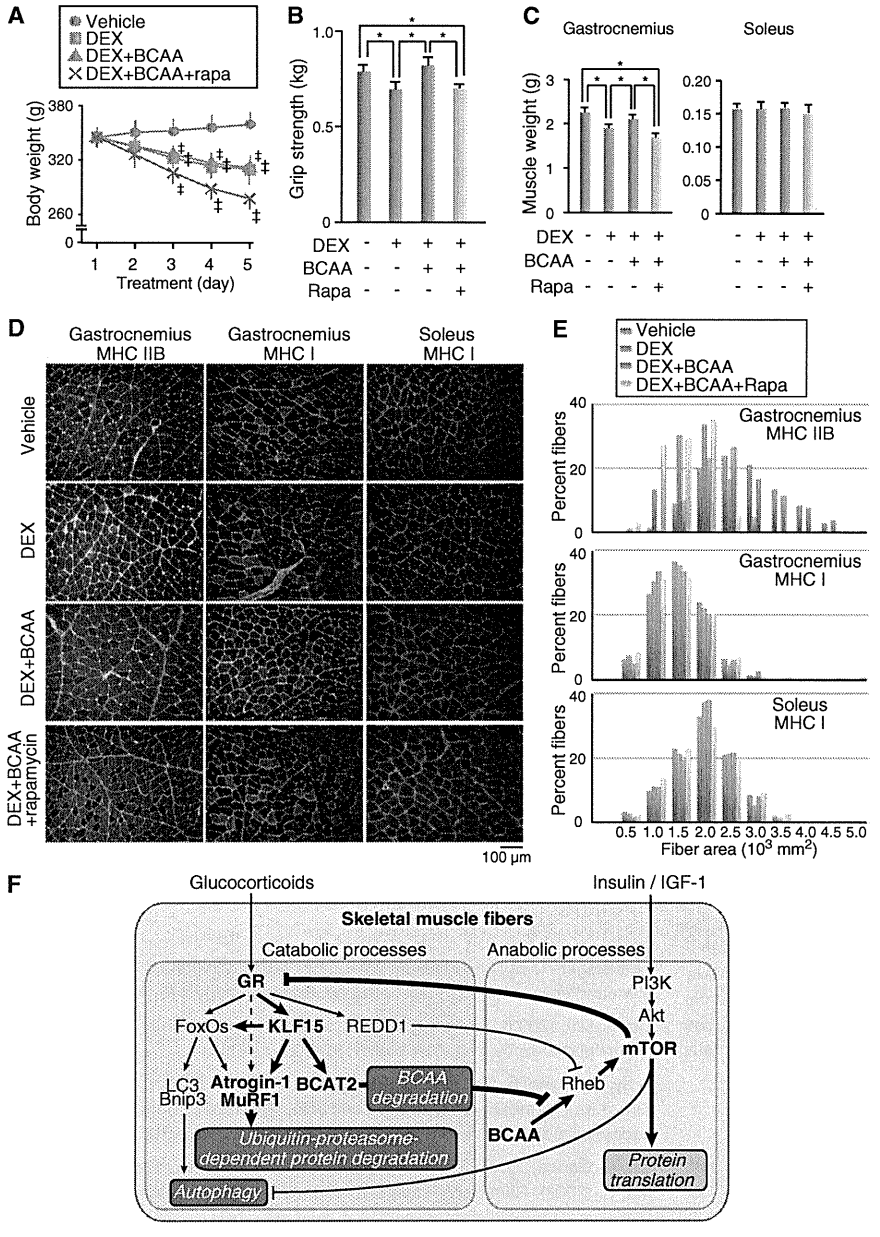

Figure 7. Restoration of Muscle Fiber Mass and Strength by mTOR Activation in DEX-Induced Skeletal Muscle Atrophy Model

(A–E) Effects of DEX, BCAA, and rapamycin on body weight (A), grip strength of forearms (B), muscle weight (C), muscle pathology (D), and CSA of skeletal muscle fiber (E). Rats were treated with DEX, BCAA, and rapamycin for 5 days as described in the Supplemental Information. (A) Time course of body weight ($n = 15$). (B) Grip strength of forearms at 5 hr after DEX injection on the day 5 ($47 < n < 51$). (C) Weight of gastrocnemius and soleus at 6 hr after DEX injection on the day 5 ($n = 15$). (D) Immunostaining for MHC IIB (red in left photographs), MHC I (red in middle and right photographs), and type IV collagen (green) of transverse cryosections. (E) CSA distribution of MHC IIB fibers (gastrocnemius) and MHC I fibers (gastrocnemius and soleus) presented as frequency histograms ($500 < n < 510$). (F) Schematic model of mutual crosstalk between catabolic processes and anabolic processes in skeletal muscle.

(A–C) Error bars show SD (A and C) or SEM (B). $^{*}p < 0.05$, $^{\dagger}p < 0.05$ versus vehicle-treated rats.

proximal part of the insulin signaling pathway (Um et al., 2006). Moreover, in obese humans, BCAA in association with a high-fat diet is linked to the elevation of insulin resistance (Newgard et al., 2009). On the other hand, it is suggested that an increase in type II fibers in obese mice may reduce fat mass and improve metabolic parameters (Izumiya et al., 2008). Therefore, it is necessary, for the validation of BCAA therapy, to evaluate the influence of long-term BCAA administration on various metabolic parameters.

In conclusion, we revealed that GR and mTOR act as catabolic and anabolic liaisons for skeletal muscle metabolism, respectively, and these molecules interact with each other at multiple levels. This issue would be of particular importance to understand the molecular mechanism underlying the regulation of the volume and metabolism of muscle and for the development of treatments for glucocorticoid-induced and wasting disorder-related skeletal muscle atrophy.

Therefore, we are convinced that the therapeutic effects of BCAA could, at least in part, be ascribed to GR inhibition by the BCAA-mediated activation of mTOR. BCAA administration also resulted in the decreased mRNA expression of autophagy-related genes (Figure 6C), indicating that this therapeutic regimen repressed the vicious circuit connecting the initial induction of GR-triggered gene expression to degradation and atrophy. Of course, we cannot rule out other mechanisms for the effects of BCAA, including the non-GR-mediated repression of atrophy and/or autophagy, and further studies are clearly needed to clarify this issue.

There are conflicting results concerning the biological effects of BCAA, e.g., the overactivation of amino acid-dependent mTOR-mediated signaling can lead to the inhibition of the

EXPERIMENTAL PROCEDURES

Rats

All animal experiments were approved by the institutional committee and conducted according to the institutional ethical guidelines for animal experiments. Rapamycin, RU486, the BCAA cocktail, and DEX administration were performed as described in the Supplemental Information. Excised tissues were snap frozen in isopentane cooled by liquid nitrogen, and crushed using Cryo-Press (Microtec, Funabashi, Japan) prefrozen in liquid nitrogen, or processed to serial 10 μm transverse cryostat sections.